

# AUTHOR QUERY FORM

	<p>Journal: Phys. Fluids</p> <p>Article Number: POF20-AR-01091</p>	<p>Please provide your responses and any corrections by annotating this PDF and uploading it to AIP's eProof website as detailed in the Welcome email.</p>
---	--	--

Dear Author,

Below are the queries associated with your article. Please answer all of these queries before sending the proof back to AIP.

**Article checklist:** In order to ensure greater accuracy, please check the following and make all necessary corrections before returning your proof.

1. Is the title of your article accurate and spelled correctly?
2. Please check affiliations including spelling, completeness, and correct linking to authors.
3. Did you remember to include acknowledgment of funding, if required, and is it accurate?

Location in article	Query/Remark: click on the Q link to navigate to the appropriate spot in the proof. There, insert your comments as a PDF annotation.
Q1	Please check that the author names are in the proper order and spelled correctly. Also, please ensure that each author's given and surnames have been correctly identified (given names are highlighted in red and surnames appear in blue).
Q2	We have removed part label (c) in the artwork of Fig. 12 in accordance with the caption and text. Please check.
Q3	Please reword the sentence beginning with "Since [ $u_2^{2D}, p_2^{2D}$ ] exactly..." so that your meaning will be clear to the reader.
Q4	We have reworded the sentence beginning "The energy levels. . ." for clarity. Please check that your meaning is preserved.
Q5	Please provide volume number in Refs. 7 and 8.
Q6	We were unable to locate a digital object identifier (doi) for Refs. 7, 8, 22, and 32. Please verify and correct author names and journal details (journal title, volume number, page number, and year) as needed and provide the doi. If a doi is not available, no other information is needed from you. For additional information on doi's, please select this link: <a href="http://www.doi.org/">http://www.doi.org/</a> .
Q7	Please provide report number in Refs. 50, 51, 66, and 71.
Q8	<p>Please provide publisher's name in Ref. 68.</p> <p>Please confirm ORCID's are accurate. If you wish to add an ORCID for any author that does not have one, you may do so now. For more information on ORCID, see <a href="https://orcid.org/">https://orcid.org/</a>.</p> <p style="margin-left: 20px;">Wasim Sarwar – 0000-0002-6430-8691</p> <p style="margin-left: 20px;">Fernando Mellibovsky – 0000-0003-0497-9052</p> <p>Please check and confirm the Funder(s) and Grant Reference Number(s) provided with your submission:</p> <p style="margin-left: 20px;">Red Espa&amp;#x00F1;ola de Supercomputaci&amp;#x00F3;n, Award/Contract Number RES-FI-2017-2-0020, Award/Contract Number RES-FI-2017-3-0009</p> <p style="margin-left: 20px;">Ministerio de Economía y Competitividad, Award/Contract Number FIS2016-77849-R</p> <p style="margin-left: 20px;">Agència de Gestió d'Ajuts Universitaris i de Recerca, Award/Contract Number 2017-SGR-00785</p> <p>Please add any additional funding sources not stated above.</p>

Thank you for your assistance.

# Characterization of three-dimensional vortical structures in the wake past a circular cylinder in the transitional regime

Cite as: Phys. Fluids 32, 000000 (2020); doi: 10.1063/5.0011311

Submitted: 21 April 2020 • Accepted: 17 June 2020 •

Published Online: XX XX XXXX



 Wasim Sarwar  and Fernando Mellibovsky<sup>a)</sup> 

## AFFILIATIONS

Department of Physics, Aerospace Engineering Division, Universitat Politècnica de Catalunya, 08034 Barcelona, Spain

<sup>a)</sup> Author to whom correspondence should be addressed: [fernando.mellibovsky@upc.edu](mailto:fernando.mellibovsky@upc.edu)

## ABSTRACT

The flow past a circular cylinder in the transitional regime at  $Re = 2000$  has been thoroughly investigated via well resolved direct numerical simulation with a spectral element code. Spanwise periodic boundary conditions of at least  $L_z \geq 2.5D$  are required to properly reproduce first and second order turbulent statistics in the cylinder wake. A Kelvin–Helmholtz instability can already be detected at this relatively low Reynolds number at the flapping shear layers issued from either side of the cylinder. The instability, with a frequency  $f_{KH} \approx 0.84$  that is in excellent agreement with published experimental results, arises only occasionally and the associated spanwise vortices are subject to spanwise localization. We show that while Kármán vortices remain predominantly two-dimensional, streamwise vortical structures appearing along the braids connecting consecutive vortices are mainly responsible for rendering the flow three-dimensional. These structures may appear in isolation or in vortex pairs and have a typical spanwise wavelength of around  $\lambda_z \approx 0.20$ – $0.28$  at a location at  $(x, y) = (3, 0.5)$ , as measured via Hilbert transform along probe arrays with spanwise orientation. In line with experimental and numerical results at higher  $Re = 3900$ , the size of the structures drops in the very near-wake to a minimum at  $x \approx 2.5$  and then steadily grows to asymptotically attain a finite maximum for  $x \gtrsim 20$ . A time-evolution-based stability analysis of the underlying two-dimensional vortex shedding flow, which happens to be chaotic, shows that the fastest growing perturbations in the linear regime have a spanwise periodicity  $\lambda_z \approx 0.3$  and are located in the very near-wake, right within the braid that connects the last forming Kármán vortex with the previous one, thus hinting at a close relation with the fully developed vortical structures observed in full-fledged three-dimensional computations.

Published under license by AIP Publishing. <https://doi.org/10.1063/5.0011311>

## I. INTRODUCTION

The incompressible viscous flow around a circular cylinder constitutes a canonical problem for the study of separated flow past bluff bodies.<sup>1</sup> A wealth of experimental and numerical studies have been conducted on this geometry over many decades, covering a wide range of flow regimes,<sup>2</sup> so as to analyze a variety of flow phenomena including laminar and turbulent boundary layer separation,<sup>3,4</sup> detached shear layer and wake instabilities,<sup>5</sup> or vortex shedding.<sup>6</sup>

The steady symmetric wake behind the cylinder destabilizes supercritically at  $Re \gtrsim 47$  ( $Re = UD/\nu$  is the Reynolds number based on cylinder diameter  $D$ , upstream flow velocity  $U$ , and fluid kinematic viscosity  $\nu$ ) into a periodic space-time-symmetric flow

regime named after von Kármán and characterized by alternate shedding of counter-rotating vortices from either side of the cylinder.<sup>7,8</sup> This unsteady regime and further transitions retaining some of its features are a source of mean aerodynamic drag increase,<sup>9,10</sup> fluid–structure resonant interaction,<sup>11,12</sup> structural vibration,<sup>13</sup> and acoustic noise.<sup>14,15</sup>

The periodic two-dimensional vortex-shedding state has been observed to persist up to  $Re \lesssim 190$ , beyond which point three-dimensionality sets in.<sup>16</sup> Two distinct three-dimensional modes have been reported in the range  $Re \in [180, 260]$  in the so-called wake-transition regime, namely, mode A and mode B. Mode A is characterized by the onset of vortex loops that are stretched by shear into streamwise vortex pairs with a spanwise wavelength of around 3 to  $4D$ . Observation of mode A has been reported from as low as

$Re \gtrsim 180$  such that it coexists with two-dimensional vortex shedding within a small  $Re$ -range, the flow behavior being hysteretical and, accordingly, the spanwise-invariance-breaking bifurcation being slightly subcritical.<sup>17</sup> Mode B occurs at a slightly higher  $Re \gtrsim 250$  with the characteristic wavelength in the order of  $1D$ <sup>18</sup> and is related to a second spanwise-invariance-breaking bifurcation of the already unstable two-dimensional periodic vortex-shedding state that occurs at  $Re \sim 259$ .<sup>10</sup> The transition from mode A to mode B involves intermittency (the flow dynamics keeps switching between the two modes) and a gradual transfer of the time-fraction of occurrence of A and B from the former to the latter. At  $Re \simeq 260$ , mode B is already the dominant structure and exhibits remarkable spanwise coherence. Besides the remarkably different spanwise wavelength, the two modes possess also distinct symmetries that tell them apart (which points at unrelated triggering instability mechanisms) and their inception is responsible for discontinuous leaps in vortex shedding frequency and characteristic slope discontinuities in the dependence of the base pressure coefficient with  $Re$ .<sup>16</sup>

On top of the small-scale structure of modes A and B, the wake transition regime also involves vortex local phase-dislocations or defects that result in intermittent large-scale spot-like structures that dominate the wake as they are advected downstream.<sup>19,20</sup> These structures are responsible for low frequency irregular fluctuations in the wake<sup>21</sup> and a discontinuous drop of vortex shedding frequency.

The shear layers resulting from boundary layer separation at either side of the cylinder are subject to turbulent transition at sufficiently high  $Re$ .<sup>22</sup> This transition follows a Kelvin–Helmholtz instability that is essentially two-dimensional and only becomes noticeable from  $Re \gtrsim 1200$ .<sup>20,23</sup> The resulting vortices accumulate downstream and are subdued into the von Kármán vortices that dominate the cylinder wake.<sup>24</sup> Based on outer velocity and boundary layer thickness at separation, a rough estimate predicts that the Kelvin–Helmholtz instability frequency must scale as  $f_{KH}/f_{vK} \sim Re^{1/2}$ ,<sup>20</sup> where the subindices in  $f_{KH}$  and  $f_{vK}$  stand for Kelvin–Helmholtz and von Kármán, respectively. A best fit to a collection of existing experimental data,<sup>20,25–27</sup> together with physical arguments as to the dependence of shear layer velocity and length scales on  $Re$ , suggests that the scaling should rather follow  $f_{KH}/f_{vK} \sim Re^{0.67}$ .<sup>23,28</sup>

The shear layers in the cylinder wake remain fairly planar only within a finite extent that is limited by the inception of the wake instability and the onset of von Kármán vortices. As a result, the Kelvin–Helmholtz instability only becomes measurable at  $Re$  sufficiently high for the vortices to reach a sufficient amplification within the limited extent for their spatial development, which can be estimated to happen for  $Re \gtrsim 1200$ .<sup>29</sup> The instability, however, must be at play from much lower  $Re$ , and the frequency scaling suggests that a resonance with the von Kármán instability is to be expected at  $Re \simeq 260$ .<sup>23</sup> As a matter of fact, this resonance has been put forward as a plausible argument for the high spanwise coherence that wake structures possess at precisely this value of  $Re$ .

It is a well established fact that both the aspect ratio and spanwise boundary conditions have an impact on the vortex shedding past a circular cylinder.<sup>30,31</sup> A systematic analysis of spanwise correlations in the three dimensional near-wake behind the cylinder reveals that structures with considerable dispersion of spanwise

wavelengths in the range  $\lambda_z \in [3, 5]D$  occur in the early wake transition regime,<sup>24,32–35</sup> dominated by mode A, in accordance with linear stability analyses.<sup>17,36</sup> The dispersion is significantly reduced when data involving dislocation are systematically discarded so that filtered measurements follow closely the maximum growth-rate mode predicted by Floquet analysis, starting at  $\lambda_z^A = 3.96D$  at onset. In the late transition regime, where mode B becomes dominant, the dispersion is much lower and wavelengths  $\lambda_z \simeq 1D$  are observed in the near-wake ( $x/D < 3$ ), close enough to the second linear instability of the already unstable two dimensional vortex shedding flow, with  $\lambda_z^B = 0.82D$ . The vortical structure spanwise size scaling in this region can be estimated as decreasing with  $1/\sqrt{Re}$ ,<sup>24</sup> which is confirmed by experiments in the range  $Re \in [300–2200]$ .<sup>33</sup> In the far wake ( $x/D > 10$ ), however, the same experiments report that the spanwise wavelength becomes fairly independent of  $Re$  and remains of order  $\lambda_z/D \sim O(1)$ .<sup>33</sup>

The variation of the spanwise wavelength of streamwise vortices along the wake at fixed  $Re$  has been analyzed both experimentally,<sup>33,37</sup> using both flow visualization and two-probe cross correlation, and numerically,<sup>38</sup> through the use of the Hilbert transform. The crossflow sampling location has a large impact on the near-wake structure length scale, which renders any comparison impractical. Sufficiently far downstream away from the cylinder, in the far wake, this effect is less noticeable and the typical wavelength is observed to clearly saturate at a fairly constant value.

There exists ample experimental evidence, backed by sound theoretical arguments, that turbulence in spatially developing flows depends, even asymptotically, on upstream conditions (i.e., the particulars of the turbulent flow generator).<sup>39,40</sup> This holds true for planar wakes<sup>41</sup> and, in particular, for the turbulent wake past a cylinder. Planar wakes past blunt bodies of characteristic blockage size  $D$  can be split in four distinct regions, namely, the near wake ( $x/D \lesssim 4$ ), the mid-wake ( $4 \lesssim x/D \lesssim 50$ ), the far wake ( $50 \lesssim x/D \lesssim 1000$ ), and the asymptotic wake ( $x/D \gtrsim 1000$ ).<sup>42</sup> The near wake is subject to direct interaction with the wake generator and bears strong correlation with aerodynamic parameters such as the base pressure coefficient or the aerodynamic forces on the body. Beyond this wake formation region, which contains the mean recirculation bubble, no action or perturbation has any measurable effect whatsoever on the flow field around the body. The mid-wake is different from the far wake in that shed vortices remain detectable, while the mean flow becomes self-similar in the far wake. A certain universality develops in the asymptotic wake, if only for conveniently scaled (with the local centerline velocity deficit and the local length scale) mean velocity profiles. Meanwhile, spreading rates and higher order turbulent moments, including Reynolds stresses, can, in principle, depend on upstream conditions.<sup>40</sup> In the case of the cylinder wake, complete self-preservation has been established experimentally at  $Re = 2000$  beyond  $x/D \gtrsim 260$ .<sup>43</sup>

While mean flow statistics are fairly independent of  $Re$  in the far wake behind a cylinder once within the shear-layer transition regime ( $Re \gtrsim 1200$ ), second order flow statistics (Reynolds stresses) only become so for  $Re \gtrsim 10\,000$ .<sup>44</sup>

There is considerable consensus as to the mid-wake flow topology within the early shear-layer transition regime, as evidenced by the good agreement across a wide range of experimental<sup>45–49</sup> and numerical<sup>49–56</sup> studies of crossflow distribution of mean velocity components at varying flow rates. Higher order flow statistics also

show reasonable agreement provided that sufficiently close  $Re$  are considered.

In the near wake, besides the fact that statistics are no longer expected to be independent of  $Re$ , results are at odds among the various experimental and numerical studies, even at coincident  $Re$ . In trying to shed light on the cause for disagreement, the flow at  $Re = 3900$  has become a recurrent benchmark case since the experiments of Lourenco and Shih<sup>45</sup> and Ong and Wallace.<sup>47</sup> Two distinct flow states have been reported, named U- and V-type after the outline of the mean streamwise velocity crossflow profile in the very near-wake of the cylinder at  $x/D = 1$ . The U-state is characterized by a longer recirculation bubble  $L_r$  (not to be confused with wake formation length); a slightly higher vortex shedding frequency  $f_{vK}$ ; a lower base pressure suction coefficient  $-C_{pb} = 2(p_\infty - p_b)/(\rho U_\infty^2)$ ; lower aerodynamic forces (mean drag  $C_D$  and root-mean-square of lift  $C_{L_{rms}} = \sqrt{\langle C_L^2 \rangle}$ ); lower Reynolds stresses  $\langle u'u' \rangle$ ,  $\langle u'v' \rangle$ , and  $\langle v'v' \rangle$ ; and characteristic double-peak distributions of  $\langle u'u' \rangle$  both in the streamwise direction along the wake centerline and in the near-wake cross-stream direction.<sup>49-51,53-56,62-64</sup> The V-state, in contrast, features a smaller  $L_r$ ; slightly lower  $f_{vK}$ ; higher  $-C_{pb}$ ,  $C_D$ ,  $C_{L_{rms}}$ , and  $\langle u'u' \rangle$ ,  $\langle u'v' \rangle$  and  $\langle v'v' \rangle$ ; and inflection plus single-peak streamwise and four-peak cross-stream distributions of  $\langle u'u' \rangle$ .<sup>45,53,54,56,62-65</sup> Table I summarizes a number of experiments, along with relevant

experimental conditions and a bunch of flow parameter results that allow characterization of the corresponding type of solution. The experiments, run at several  $Re \sim O(10^3)$  on experimental setups of different spanwise extent, include Particle Image Velocimetry (PIV), Laser Doppler Velocimetry (LDV), and Hot Wire Anemometry (HWA) measurements, and varying levels of free-stream turbulence ( $Tu$ ). Statistics have been collected over variable counts of vortex shedding cycles. It becomes clear from the flow parameter values that V-type solutions are favored at large  $Re$  or in the presence of higher  $Tu$ , U-type profiles being ubiquitous for sufficiently low  $Re$  and low  $Tu$  experiments. These studies also seem to point at a gradual transition from one state to the other as  $Re$  is increased in the same experimental setup with all other parameters kept constant.

Table II contains an extensive list of numerical simulations of the flow past a circular cylinder at Reynolds numbers relevant to the regime under scrutiny. Summarized alongside the main results (to be compared with the experimental results of Table I) are the most significant simulation parameters such as the numerical method used, the spanwise periodic extent of the domain, the in-plane and spanwise resolutions (and order of the discretization), and the number of vortex shedding cycles collected for statistics. The in-plane domain size and the time discretization method and order

**TABLE I.** Literature review of experimental results for the flow past a circular cylinder. Reported are, when available, the flow measurement method (HWA: hot wire anemometry; PIV: particle image velocimetry; LDV: laser Doppler velocimetry), preturbulence level  $Tu$ , Reynolds number  $Re$ , cylinder span size  $L_z$ , number of vortex shedding cycles recorded for statistics  $N_s$ , von Kármán frequency  $f_{vK}$ , Kelvin–Helmholtz frequency  $f_{KH}$ , wake instability frequency  $f_w$ , recirculation bubble length  $L_r$ , mean drag coefficient  $C_D$  and rms fluctuation  $C'_D$ , lift coefficient rms fluctuation  $C'_L$ , base pressure coefficient  $-C_{pb}$ , and location of the boundary layer separation  $\theta_{sep}$ .

Experimental															
Author (references)	Method	$Tu$ (%)	$Re$	$L_z$	$N_s$	$f_{vK}$	$f_{KH}$	$f_w$	$L_r$	$C_D$	$C'_D$	$C'_L$	$-C_{pb}$	$\theta_{sep}$	
Norberg <sup>27</sup>	HWA	0.1	2 000	240	?	0.213									
		0.1	3 000	80		0.213			1.65	0.98			0.84		
		1.4	3 000	80		0.209			1.44	1.03				0.89	
		0.1	8 000	80		0.204			0.99	1.13				1.05	
		1.4	8 000	80		0.199			0.90	1.20				1.12	
Lourenco and Shih <sup>45</sup>	PIV	?	3 900	21	29				1.18	0.98				$85 \pm 2$	
Ong and Wallace <sup>47</sup>	HWA	0.67	3 900	84	7680	0.21									
Norberg <sup>48</sup>	LDV	<0.1	1 500	65	1350				1.79						
		<0.1	3 000	65					1.66						
		<0.1	5 000	65					1.40						
		<0.1	8 000	65					1.17						
		<0.1	10 000	65					1.02						
Norberg <sup>57</sup>	LDV	<0.1	1 500	105	?	0.212						0.045			
		<0.1	4 400	105		0.210						0.100			
Konstantinidis <i>et al.</i> <sup>58</sup>	LDV	3.3	1 550	10	?										
		3.3	2 150	10		0.215			1.77						
		3.3	2 750	10											
		3.3	7 450	10											
Konstantinidis <i>et al.</i> <sup>59</sup>	PIV	3.3	2 160	10	?										
Konstantinidis and Balabani <sup>60</sup>	PIV	3	2 150	10	?	0.215			1.58						
Dong <i>et al.</i> <sup>61</sup>	PIV	?	4 000	8.78	?				1.47						
Parnaudeau <i>et al.</i> <sup>49</sup>	PIV	<0.2	3 900	20	250				1.51						
	HWA	<0.2	3 900	20	2856	0.208									

237 **TABLE II.** Literature review of numerical results for the flow past a circular cylinder. Besides some of the parameters reported in Table I, listed are the numerical method employed  
 238 (DNS: direct numerical simulation; LES: Large Eddy simulation; FVM: Finite Volume Method; FDM: Finite Difference Method; SEM: Spectral Element Method; SDM: Spectral  
 239 Difference Method), the spanwise periodic extent of the domain  $L_z$ , the in-plane  $N_{xy}$  and spanwise  $N_z$  resolutions (the superindex indicates discretization order,  $F$  for Fourier),  
 240 and near wake solution topology Sol (U: U-state; V: V-state; UV: mixed; ?: inconclusive).  
 241

Numerical														
Author (references)	Method	$Re$	$L_z$	$N_z$	$N_{xy}$	$N_s$	$f_{vK}$	$f_{KH}$	$f_w$	$L_r$	$C_D$	$-C_{p_b}$	$\theta_{sep}$	Sol.
242 Present results: Case 1	DNS SEM	2000	1.5	64	4 040 <sup>8</sup>	66	0.218	1.237		1.50	1.015	0.88	92.0	U
243 Case 2			2	64	4 040 <sup>8</sup>	58	0.212	1.121		1.58	0.987	0.83	90.3	U
244 Case 3			2.5	128	5 484 <sup>8</sup>	55	0.215	0.839		1.66	0.975	0.80	90.0	U
245 Case 4			$\pi$	96	5 484 <sup>8</sup>	22	0.211			1.71	0.961	0.79	90.0	U
246 Lehmkuhl <i>et al.</i> <sup>56</sup>	DNS FVM	3900	$\pi$	128	72 700	858	0.215	1.34	0.0064	1.36	1.015	0.935	88	UV
						L:250	0.218			1.55	0.979	0.877	87.8	U
						H:250	0.214			1.26	1.043	0.98	88.3	V
			$2\pi$	256		330	0.214			1.363	1.019	0.933		UV
248 Gsell <i>et al.</i> <sup>38</sup>	DNS FVM	3900	10	300	150 000	3–4	0.21	1.365			0.92		86.8	
249 Kravchenko and Moin <sup>54</sup>	LES FDM	3900	$\pi$	48 <sup>F</sup>	27 780 <sup>S</sup>	7	0.21			1.35	1.04	0.93	88	UV
				8			0.193			1.00	1.38	1.23		V
				48	10 570		0.206			1.04	1.07	0.98		V
			$\pi/2$	24	27 780		0.212			1.30	1.07	0.97		UV
250 Ma <i>et al.</i> <sup>53</sup>	DNS SEM	3900	$\pi$	128 <sup>F</sup>	902 <sup>10</sup>	?	0.219			1.59		0.84		U
			$1.5\pi$	64 <sup>F</sup>	902 <sup>10</sup>		0.206			1.00		1.04		V
			$2\pi$	256 <sup>F</sup>	902 <sup>8</sup>		0.203			1.12		0.96		V
251 ( $c_s = 0.032$ )	LES SEM		$1.5\pi$	64 <sup>F</sup>	902 <sup>8</sup>		0.213			1.28		0.898		UV
252 ( $c_s = 0.196$ )			$1.5\pi$	64 <sup>F</sup>	902 <sup>8</sup>		0.208			1.76		0.765		U
253 Mittal <sup>66</sup>	LES FDM	3900	$\pi$	48	39 900	7	~0.21				1.1	1.15	88	U?
					32 900						1.2	1.28	89	U?
254 Mittal <sup>51</sup>	LES FDM	3900	$\pi$	48 <sup>F</sup>	48 120	12				1.40	1.0	0.93	86.9	UV?
										1.36	1.0	0.95	85.8	UV?
255 Breuer <sup>52</sup>	LES FVM	3900	$\pi$	64	27 225	>22	0.215		~0.007	1.372	1.016	0.941	87.4	UV
							0.215			1.043	1.097	1.069	88.5	V
							0.215			1.686	0.969	0.867	86.7	U
							0.215			1.115	1.099	1.049	87.9	V
			$2\pi$	64			0.215			1.114	1.089	1.036	87.9	V
256 Franke and Frank <sup>55</sup>	LES FVM	3900	$\pi$	33	35 584	42	0.209			1.64	0.978	0.85	88.2	U
257 Dong <i>et al.</i> <sup>61</sup>	DNS SEM	3900	$\pi$	128 <sup>F</sup>	902 <sup>8</sup>	40–50	0.21?	1.539		1.36				UV
			$1.5\pi$	192 <sup>F</sup>	902 <sup>8</sup>		0.208			1.18		0.93		V
				128 <sup>F</sup>			0.210			1.12		0.96		V
				64 <sup>F</sup>			0.206			1.00		1.04		V
258 Chen <i>et al.</i> <sup>64</sup>	iLES FVM	2580	$\pi$	56	70 000	50	0.22			1.66	0.95	0.73		U
				20	12 500	50	0.22			1.13	1.03	0.88		V
259 Mohammad <i>et al.</i> <sup>67</sup>	iLES SDM	2580	$\pi$	18 <sup>3</sup>	11 144 <sup>3</sup>	20								U
				18 <sup>2</sup>	7 880 <sup>2</sup>	20								V
				12 <sup>3</sup>	7 880 <sup>3</sup>	20								U
260 Lodato and Jameson <sup>68</sup>	iLES SDM	2580	3.2	10 <sup>3</sup>	1 847 <sup>3</sup>	300								U
261 Lodato and Jameson <sup>69</sup>	DNS FVM	3300	4	512	416 556	10	0.214						87.3	U
262				256	63 336		0.216						90.3	V
263			8	1024	416 556		0.216						87.4	U
264 Beaudan and Moin <sup>50</sup>	DNS FDM	3900	$\pi$	48 <sup>5</sup>	19 584 <sup>5</sup>	6	0.216			1.56	0.96	0.89	85.3	U
265 Tremblay <sup>65</sup>	DNS FVM	3900	$\pi$	112	419 364	60	0.22			1.3	1.03	0.93	85.7	UV

266 have been deemed appropriate for all cases and are therefore not  
267 reported. In the case of large eddy simulations (LESs), the model  
268 and/or subgrid-scale dissipation parameter  $c_s$  are also reported.  
269 The last column indicates whether the reported results feature a  
270 U-type or V-type cross-stream velocity profile in the near wake  
271 and/or the statistically averaged results are compatible with one or  
272 the other. UV indicates results that appear to be halfway between  
273 U- and V-type states, while the question mark denotes inconclusive  
results.

274 There has been much controversy as to whether there naturally  
275 exists a unique near wake topology or if both states may occur, under  
276 what circumstances should one or the other be expected.

277 Based on  $L_r$  and  $C_{pb}$  as indirect indicators, a gradual transi-  
278 tion from the U-state toward the V-state with the increase in  
279  $Re$  has been reported by several experimental studies.<sup>27,70–72</sup> The  
280 U-state would seem to dominate at  $Re \sim 2000$ , while the V-state  
281 has completely taken over from  $Re \gtrsim 10000$ . This trend has been  
282 later confirmed by direct measurement of mean and second order  
283 flow statistics in the near wake of the cylinder.<sup>48</sup> Increased pre-  
284 turbulence levels  $Tu$  have been shown to shift the gradual transi-  
285 tion to slightly lower  $Re$ -values,<sup>27</sup> while an insufficient cylinder  
286 aspect ratio  $L_z/D$ , such that the spanwise boundary conditions drive  
287 the flow, has a stabilizing effect for the U-state.<sup>31</sup> This suggests  
288 that the spanwise size of near-wake structures might be playing  
289 an important role in near-wake flow statistics as numerics seem  
290 to substantiate.<sup>53,61,69</sup> Simulations are usually undertaken with peri-  
291 odic boundary conditions in the spanwise direction, and an insuffi-  
292 cient spanwise domain size ( $L_z/D \leq \pi$  at  $Re = 3900$ ) has been  
293 shown to favor the U-state, with all other parameters kept constant.  
294 The V-state can however be artificially recovered in small domains  
295 when the spanwise direction is under-resolved<sup>51,52,54,62,63,66</sup> allegedly  
296 due to insufficient viscous dissipation of turbulent kinetic energy.  
297 The same applies to overly coarse in-plane resolutions, which also  
298 result in V-state selection.<sup>54,64</sup> In the case of LES simulation, over-  
299 dissipative subgrid scale models also tend to induce the U-state  
300 even in domains of allegedly sufficient spanwise extent,<sup>53,64</sup> while  
301 under-dissipative models induce V-type profiles in short spanwise  
302 domains.<sup>62–64</sup>

303 The large scatter of results, which yield conflicting values for  
304 most of the mean integral quantities, has occasionally been ascribed  
305 to unconverged statistics due to exceedingly short time series of data  
306 (insufficient sample size),<sup>55,62</sup> although this alone cannot explain all  
307 of the observed discrepancies. A statistical analysis of near wake  
308 velocity time series from direct numerical simulation, spanning over  
309 800 vortex shedding cycles, detected a very low frequency of about  
310 3 of the Strouhal number that was traced back to an instability of  
311 the mean recirculation bubble size.<sup>56</sup> Conditional and phase averag-  
312 ing revealed that the mean statistics might be in fact the weighted  
313 mean of two modes, a high and a low energy mode, correspond-  
314 ing to the V-state and U-state, respectively. In this light, the scat-  
315 ter of inconsistent results would be a consequence of averaging  
316 too short time series at different phases along the low frequency  
317 cycle. The low-pass filtered signals do not consist of memoryless  
318 intermittent switching between the two so-called modes such that  
319 the scenario of two strange saddles linked by heteroclinic connec-  
320 tions can be discarded altogether. The temporal dynamics would  
321 rather correspond to an instability of a unique state, although fur-  
322 ther inquiry shall be required to test this hypothesis. In any case, the

physical mechanism underlying the low frequency evolution of the  
near wake remains unaccounted for. The loopback mechanism by  
which the high energy short recirculation bubble should progress  
toward a lower energy longer bubble and then back remains a mys-  
tery. Even though the unconverged statistics issue might apply to  
almost all preceding numerical studies and a few of the experi-  
ments,<sup>45</sup> most experimental studies analyze sufficiently long data  
series that the low frequency could have been detected and the  
mean state obtained.<sup>27,48,49,58,61</sup> Instead, U-type near wake statistics  
are reported in most cases.

All things considered, it would seem that there is in fact a grad-  
ual shift from U- to V-type near wake statistics as  $Re$  is increased and  
that the former is still dominant at  $Re = 3900$ . Observation of V-type  
short recirculation bubbles would therefore be an artifact of either  
biased statistics or, in the case of numerical simulation, too coarse a  
resolution to capture the dissipative length scales.

We shall focus here on the cylinder shear layers and wake  
regime at  $Re = 2000$ , with the intention of probing the occurrence  
of the U- and V-states when the Kelvin–Helmholtz instability is per-  
ceptible but sufficiently weak that turbulent statistics are modest  
in the near wake. The reason for this choice of Reynolds number  
is threefold. To begin with, the experiments by Norberg provide  
the most accurate experimental results at the lowest  $Re$  at which  
the shear layer instability has been consistently reported. It was  
our intention to get as far down from  $Re = 3900$  as possible to  
avoid the low frequency wake oscillation reported by Lehmkuhl  
*et al.*<sup>56</sup> but still guarantee the detection of the shear layer instabil-  
ity. Finally, the stability analysis of the underlying two-dimensional  
chaotic flow to three-dimensional perturbations could not be pushed  
much further beyond  $Re = 2000$ , as pseudo-modal growth becomes  
so fast that the methods used become unsuitable. Procuring the  
fastest-growing three-dimensional pseudo-modes for comparison  
with fully resolved computational results requires that  $Re$  be kept  
sufficiently low. Comparison with  $Re = 3900$  will be established once  
the simulation has been calibrated against experimental<sup>23,27,48,57–59,73</sup>  
and numerical<sup>64,67–69</sup> data at  $Re \in [1500–3000] \sim 2000$ , with the  
objective of gaining some insight on the effects of Reynolds num-  
bers on near-wake turbulent statistics in the early transitional flow  
past the cylinder.

The outline of the manuscript is as follows. The mathematical  
formulation is presented in Sec. II alongside the numerical approach  
undertaken to solve the equations. Section III reports the numer-  
ical results in terms of global quantities first, followed by near-  
and mid-wake turbulent statistics. The instability of the shear layers  
that flap in the near-wake is investigated in Sec. IV, together with  
the characterization, in terms of location and spanwise size, of the  
vortical structures that are responsible for the three-dimensionality  
of the cylinder wake. The stability analysis of the underlying two-  
dimensional flow is also undertaken in order to determine the nature  
of the fastest growing perturbations for comparison against the  
vortical structures observed in full three-dimensional simulations.  
Finally, the main findings are summarized in Sec. V.

## II. PROBLEM FORMULATION AND NUMERICAL APPROACH

The incompressible flow around an infinitely long spanwise-  
aligned circular cylinder is governed by the Navier–Stokes

379 equations, which, after suitable nondimensionalization with cylinder diameter  $D$  and upstream flow velocity  $U$ , read as  
 380

$$381 \quad \frac{\partial \mathbf{u}}{\partial t} + (\mathbf{u} \cdot \nabla) \mathbf{u} = -\nabla p + \frac{1}{Re} \nabla^2 \mathbf{u}, \quad (1)$$

$$382 \quad \nabla \cdot \mathbf{u} = 0,$$

384 where  $\mathbf{u}(\mathbf{r}; t) = (u, v, w)$  and  $p(\mathbf{r}; t)$  are the nondimensional velocity and pressure, respectively, at nondimensional location  $\mathbf{r} = (x, y, z)$   
 385 and advective time  $t$ .  $x$  ( $u$ ),  $y$  ( $v$ ), and  $z$  ( $w$ ) denote the stream-  
 386 wise, crossflow, and spanwise coordinates (velocity components),  
 387 respectively.  $Re = UD/\nu$  is the Reynolds number. The domain in  
 388 the streamwise-crossflow plane takes  $(x, y) \in [-20, 50] \times [-20, 20]$   
 389 (see Fig. 1), while periodic boundary conditions  $[\mathbf{u}, p](\mathbf{r} + L_z \hat{\mathbf{k}}; t)$   
 390  $= [\mathbf{u}, p](\mathbf{r}; t)$  are assumed in the spanwise direction with period-  
 391 icity length  $L_z = 1.5, 2, 2.5$  and  $\pi$ . The spanwise domain extent  
 392 has been chosen to fit a minimum of three typical spanwise struc-  
 393 tures (streamwise vortex pairs) in the near wake, as estimated by  
 394 the empirical scaling  $\lambda_z \sim 20Re^{-0.5}$  at  $x = 3$ .<sup>33</sup> The size of the struc-  
 395 tures is known to grow along the wake<sup>33,47</sup> but not as much as to  
 396 not fit in the computational domain. The boundary conditions for  
 397 velocity are unitary Dirichlet at the upstream boundary  $\mathbf{u}(-20, y, z)$   
 398  $= \hat{\mathbf{i}}$ , non-slip on the cylinder wall  $\mathbf{u}_w = 0$ , slip wall on the upper  
 399 and lower boundaries  $\partial_y u(x, \pm 20, z) = v(x, \pm 20, z) = \partial_y w(x, \pm 20, z)$   
 400  $= 0$ , and homogeneous Neumann at the downstream boundary  $(\nabla \cdot \mathbf{u} \cdot \hat{\mathbf{n}})(50, y, z) = 0$ . For pressure, high-order homogeneous Neumann  
 401 boundary conditions are applied everywhere except for the down-  
 402 stream boundary, where homogeneous Dirichlet conditions  $p(50, y, z) = 0$  are imposed. The high-order pressure Neumann bound-  
 403 ary conditions are designed consistent for the splitting scheme used  
 404 in the time-discretization.<sup>74</sup> Convective-type boundary conditions  
 405 were considered for the downstream boundary, but as they slowed  
 406 down the computations while producing no measurable impact  
 407 on the cylinder wake dynamics, they were discarded altogether  
 408 on account of the sufficient streamwise extent of the downstream  
 409 domain.

410 The flow has been evolved in time using the incompressible  
 411 Navier–Stokes solver of the tensor-product-based spectral/finite ele-  
 412 ment package Nektar++.<sup>74</sup> Spatial discretizations of  $K = 4040$  and  
 413  $5484$  high-order quadrilateral elements have been employed in the

417 streamwise-crossflow plane, with Lagrange polynomial expansions  
 418 up to order  $P - 1 = 7$ . A continuous Galerkin projection has  
 419 been enforced across element boundaries. A particularly refined  
 420 mesh has been set up in the vicinity of the cylinder, as shown in  
 421 the inset of Fig. 1, to properly resolve boundary layers and sep-  
 422 aration, as well as in the near wake, where turbulent fluctuations  
 423 may have significant impact on the flow field topology around the  
 424 cylinder. Fourier expansions with resolutions ranging from  $N_z =$   
 425  $\pm 64$  to  $\pm 128$  modes have been deployed in the periodic spanwise  
 426 direction along with Orszag’s 3/2 rule for dealiasing. In order for  
 427 the discrete operators to preserve the symmetries of their contin-  
 428 uous counterparts, the advection term has been written in skew-  
 429 symmetric form. For the time discretization, a second order velocity-  
 430 correction splitting scheme with a time step  $\Delta t = 0.0002$  has been  
 431 adopted as providing sufficient time-integration accuracy. Larger  
 432 time steps might have sufficed accuracy-wise, but the discrete oper-  
 433 ators resulting from the second order implicit–explicit (IMEX)  
 434 splitting-scheme employed are stiff and trigger numerical instabil-  
 435 ity for  $\Delta t$  beyond that used. Fully implicit time-discretization  
 436 schemes might be used with much larger time steps at the cost of  
 437 having to solve extremely large nonlinear systems of equations at  
 438 every time step, which renders the time evolution extremely slow  
 439 and, in our case, unfeasible from a memory storage requirement  
 440 perspective.

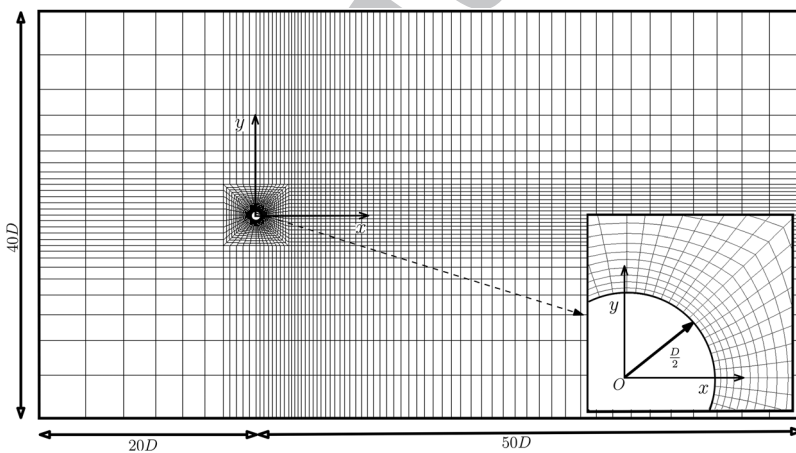
441 The instantaneous velocity field has been split following

$$442 \quad \mathbf{u}(\mathbf{r}; t) = \bar{\mathbf{u}}(\mathbf{r}_2) + \underbrace{\mathbf{u}'_2(\mathbf{r}_2; t) + \mathbf{u}_3(\mathbf{r}; t)}_{\mathbf{u}'(\mathbf{r}; t)}, \quad (2)$$

443 where  $\mathbf{r}_2 = (x, y)$  and  $\bar{\mathbf{u}} = (\bar{u}, \bar{v}) = \langle \mathbf{u} \rangle_{zt}$  is the spanwise- and  
 444 time-averaged two-dimensional mean velocity field.  $\mathbf{u}' = (u', v', w')$   
 445 is the time-dependent (fluctuating) velocity field. The von Kármán  
 446 spanwise vortex shedding mode is represented by

$$447 \quad \mathbf{u}'_2(\mathbf{r}_2; t) = \mathbf{u}_2(\mathbf{r}_2; t) - \bar{\mathbf{u}}(\mathbf{r}_2), \quad (3)$$

448 with  $\mathbf{u}_2(\mathbf{r}_2; t) = \langle \mathbf{u} \rangle_z$  as the spanwise-averaged instantaneous two-  
 449 dimensional velocity field. Finally,  $\mathbf{u}_3 = \mathbf{u} - \mathbf{u}_2$  represents the purely  
 450 three-dimensional perturbation velocity field. The Reynolds stress



451 **FIG. 1.** Sketch of the computational domain and mesh. The  
 452 streamwise-crossflow  $x$ – $y$  plane is discretized in high-order  
 453 spectral quadrilateral elements, while the spanwise direc-  
 454 tion uses a Fourier expansion. The inset shows a detail of  
 455 the mesh around the cylinder and in the near wake.

456 tensor is defined to include fluctuations both due to von Kármán  
457 vortex shedding and the three-dimensional deviation away from it,

$$458 \quad -\langle \mathbf{u}' \otimes \mathbf{u}' \rangle = -\begin{pmatrix} \langle u'u' \rangle & \langle u'v' \rangle & \langle u'w' \rangle \\ \langle v'v' \rangle & \langle v'v' \rangle & \langle v'w' \rangle \\ \langle w'w' \rangle & \langle w'v' \rangle & \langle w'w' \rangle \end{pmatrix}. \quad (4)$$

461 **III. RESULTS**

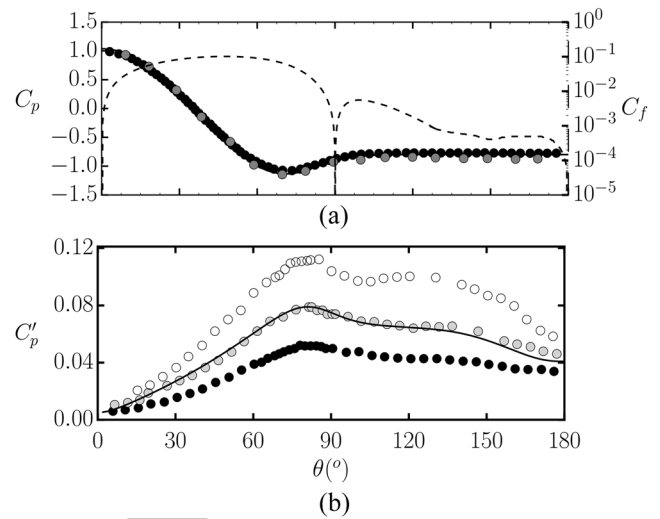
462 **A. Global quantities**

463 The most salient global quantities that result from our numerical  
464 simulations are listed in Table II. The statistics are deemed sufficient-  
465 ly converged for cases 1 through 3, while case 4 may require  
466 longer runs. Partial analysis of increasingly long time-samples shows  
467 that a bare minimum of 30–40 vortex shedding cycles are required  
468 for converged turbulent statistics. This is true of our computations  
469 at  $Re = 2000$  but cannot be extrapolated to higher Reynolds numbers,  
470 which may require somewhat longer simulation times. Cases  
471 3 and 4 have enhanced in-plane resolution with respect to 1 and  
472 2 (5484 against 4040 seventh-order spectral elements), while spanwise  
473 resolution is highest for case 3 (~50 Fourier modes per spanwise  
474 unit), followed by case 1 (~42), case 2 (~32), and case 4 (~31). The  
475 lowest resolutions used here qualify as broadly adequate in view of  
476 the published literature, and all other parameters being kept constant,  
477 only further coarsening had an observable effect on statistics.  
478 On the other hand, increasing the spanwise size of the domain from  
479  $L_z = 1.5$  (case 1) to 2.5 (case 3) does have a noticeable impact on  
480 all global quantities, while further increase to  $L_z = \pi$  has little to  
481 no effect. We will therefore focus the analysis on case 3 as it gathers  
482 the highest resolution, seemingly adequate spanwise extent, and  
483 the sufficiently long time integration that is required to produce well  
484 converged statistics.

485 Vortex shedding frequency  $f_{vK} = 0.215$  stands in perfect agree-  
486 ment with experiments both at the same or nearby Reynolds  
487 number<sup>27,58,60</sup> and at noticeably higher  $Re$ ,<sup>27,47,49,57</sup> given that  
488 the evolution of the Strouhal number in this regime is rather flat.<sup>31</sup>

489 The mean drag coefficient has not often been reported in exper-  
490 iments, but our result  $C_D = 0.975$  is in very close agreement with  
491 the few cases where it has.<sup>27,45</sup> Consistency with numerical simu-  
492 lations at similar  $Re$  is also good,<sup>64</sup> and the somewhat higher values  
493 reported at the very common  $Re = 3900$  are entirely compatible with  
494 the slightly increasing trend expected in this regime. The lift coeffi-  
495 cient rms fluctuations  $C_L' = 0.102$  fall within the range reported in  
496 the only experiments where these have been measured.<sup>57</sup>

497 The distribution of the mean pressure coefficient  $C_p(\theta)$  (solid  
498 line) along the cylinder wall is shown in Fig. 2(a). The stagnation  
499 point, clearly identifiable with  $C_p(0) = 1$  at  $\theta = 0^\circ$ , is followed by  
500 a quick descent of  $C_p$  as the flow accelerates and reaches a mini-  
501 mum at  $\theta \simeq 70.7^\circ$ . Here, recompression starts and separation occurs  
502 shortly after at  $\theta_{sep} = 90.0^\circ$ , as indicated by the null mean fric-  
503 tion coefficient  $C_f = 2\tau_w/(\rho U_\infty)$  (dashed line;  $\tau_w$  is the wall shear  
504 stress). Beyond the mean separation point,  $C_p$  keeps increasing but  
505 quickly saturates at the cylinder base value  $C_{pb} = -0.80$  such that the  
506 distribution becomes flat. Meanwhile,  $C_f$  quickly recovers beyond  
507 separation except that friction acts in the upstream direction and  
508 then decreases non-monotonically down to null at the base of the  
509 cylinder. The  $C_p$  distribution compares favorably with experiments.  
510 The numerical results closely follow those of Norberg,<sup>31</sup> measured



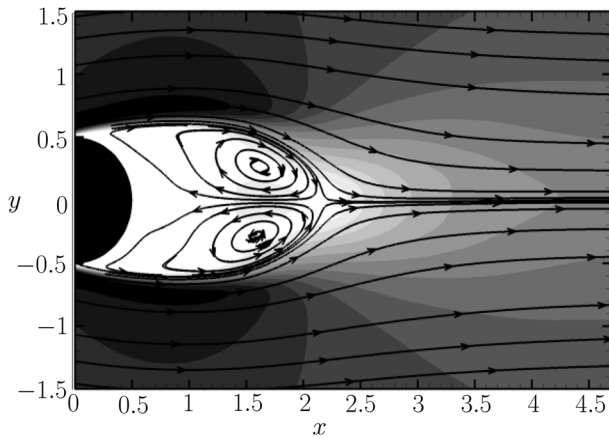
511 **FIG. 2.** (a) Mean pressure coefficient  $C_p$  (left axis, solid) and skin friction  $C_f$  (right  
512 axis, dashed) coefficient distributions on the cylinder surface. Also shown are  
513 experimental distributions of  $C_p$  by Ref. 31 (black circles:  $Re = 1500$ , aspect ratio  
514 50) and Ref. 27 (dark gray circles:  $Re = 3000$ ). (b) rms fluctuation of the pressure  
515 coefficient  $C_p'$ . Circles indicate the experimental results by Ref. 57 at  $Re = 1500$   
516 (black), 4400 (light gray), and 5000 (white).

517 at  $Re = 1500$ , while the boundary layer remains attached. The com-  
518 puted flat  $C_p$  distribution in the detached region falls precisely in  
519 between experiments at  $Re = 1500$ <sup>31</sup> and  $Re = 3000$ .<sup>27</sup> The higher  
520 values reported at  $Re = 3900$  obey the known increasing trend of  
521  $-C_{pb}$  beyond  $Re \gtrsim 2000$ .<sup>1,31</sup> The rms fluctuation of the pressure  
522 coefficient  $C_p'$  is shown in Fig. 2(b). Fluctuations are almost imper-  
523 ceptible at the stagnation point and rise steadily along the front  
524 surface of the cylinder. They peak at  $\theta \simeq 82^\circ$ , just ahead of the  
525 boundary layer separation point. Beyond this point, they remain  
526 fairly high although a slight decreasing trend is observed as the  
527 cylinder base is approached. Comparison with the experiments by  
528 Norberg<sup>57</sup> is fair. The functional shape is closely mimicked by our  
529 numerical results, and a quantitative comparison places our  $Re =$   
530 2000 results in between the experimental results at  $Re = 1500$  (black  
531 circles) and  $Re = 5000$  (empty circles). Very close agreement is  
532 achieved with experiments at  $Re = 4400$  (light gray circles), but  
533 whether this is a result of experimental or numerical inaccuracies  
534 or reveals actual physics consisting of a  $C_p'$  plateau in the range  
535  $Re \in [2000-4400]$  is a question that cannot be elucidated from existing  
536 data.

537 The separation point, at  $\theta_{sep} = 90.0^\circ$ , is slightly retarded with  
538 respect to numerical simulations at  $Re = 3900$  reported in the liter-  
539 ature (see Table 1). The only experimental attempt at measuring it  
540 produced a value  $\theta_{sep} = 85 \pm 2$  at  $Re = 3900$ , while no numerical or  
541 experimental study has ever reported it for  $Re = 2000$  to the authors'  
542 knowledge.

542 **B. Near-wake topology and statistics**

543 The near-wake mean velocity field  $\bar{\mathbf{u}}(\mathbf{r}_2)$  consists in a  
544 closed recirculation bubble, as illustrated by the mean flow-field



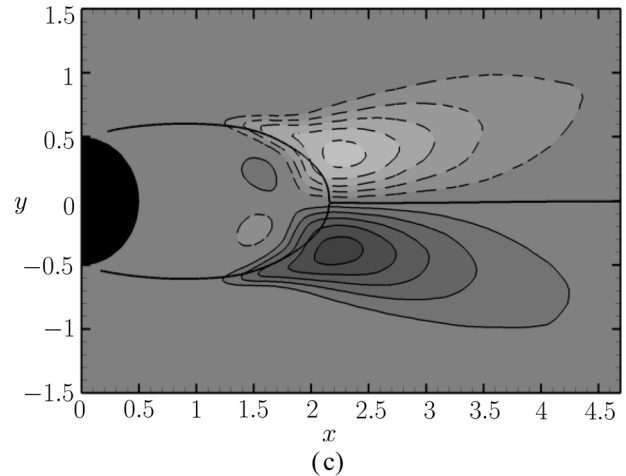
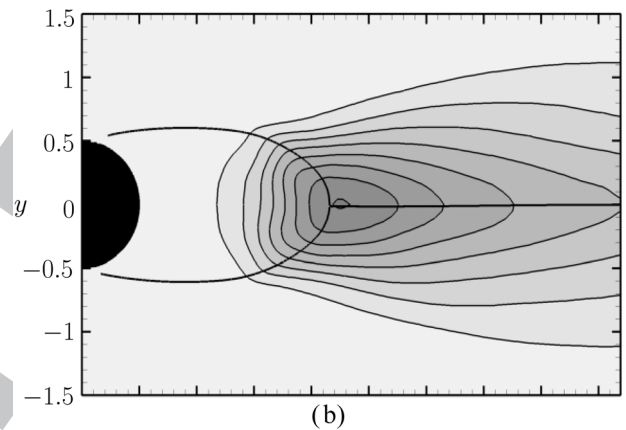
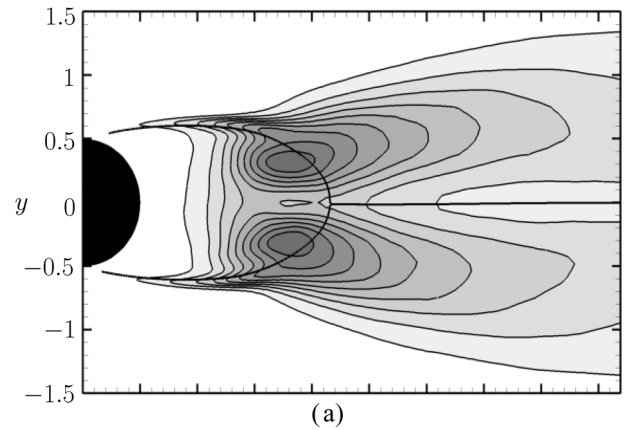
545 **FIG. 3.** Near-wake mean flow topology. Velocity magnitude contour plot, with  
 546  $\|\bar{\mathbf{u}}\| \in [0.0, 1.3]$  [darker shading for higher velocity] in steps  $\Delta\|\bar{\mathbf{u}}\| = 0.1$ , and  
 547 streamlines.

548 streamlines in Fig. 3. Within the enclosed recirculation bubble,  
 549 delimited at the rear by a stagnation point, a symmetric vortex pair  
 550 is clearly discernible. The streamline distribution compares favorably with the PIV  
 551 measurements by Konstantinidis and Balabani<sup>60</sup> [Fig. 2(a)] for a steady cylinder at  $Re = 2150$ , as also do the time-  
 552 averaged velocity magnitude contours. The high cross-stream gradients of the velocity  
 553 magnitude along the top and bottom boundaries of the recirculation bubble indicate the  
 554 presence of strong shear layers. The statistical symmetry with respect to the wake  
 555 centerline is clear, which constitutes a good indicator that the data samples are  
 556 sufficiently large.

559 Contour plots of second-order flow statistics are shown in  
 560 Figs. 4(a)–4(c). The normal-streamwise [ $\langle u'u' \rangle$ , Fig. 4(a)] and  
 561 streamwise-cross-stream Reynolds stresses [ $\langle u'v' \rangle$ , Fig. 4(c)] have  
 562 symmetric and anti-symmetric extrema, respectively, away from  
 563 the wake centerline. While  $\langle u'u' \rangle_{\max}$  occurs at the rear part but  
 564 still within the recirculation bubble,  $\langle u'v' \rangle_{\min}$  falls right outside the  
 565 bubble closure. Both Reynolds stresses peak right in the vortex  
 566 formation region, and their contours extend upstream along the shear  
 567 layers separated from either side of the cylinder. The maximum  
 568 cross-stream normal Reynolds stress [ $\langle v'v' \rangle$ , Fig. 4(b)] occurs on the  
 569 wake centerline just beyond the downstream boundary of the  
 570 recirculation bubble. Qualitative agreement with the PIV measurements  
 571 by Konstantinidis and Balabani<sup>60</sup> [Fig. 4(a)] is fair. The statistical  
 572 symmetry of Reynolds stress distribution is also accomplished. The  
 573 maximum spanwise normal Reynolds stress ( $\langle w'w' \rangle$ , not shown)  
 574 occurs also on the wake centerline.

575 Table III reports extrema and streamwise location of near-wake  
 576 flow-field statistics along the wake centerline, corresponding to current  
 577 simulations and several experimental and numerical published results.

578 Cases 1 and 2, corresponding to rather short spanwise domains,  
 579 feature rather small maximum velocity defect ( $1 - \bar{u}_{\min}$ ) along  
 580 the wake centerline at a location relatively close to the cylinder  
 581 base, comparable to that reported in the literature at higher  
 582 Reynolds numbers of  $Re \approx 3900\text{--}4000$ .<sup>48,49,54,61</sup> Cases 3 and 4 have



583 **FIG. 4.** Near-wake Reynolds stresses. (a)  $\langle u'u' \rangle \in [0.0, 0.32]$  in steps  $\Delta\langle u'u' \rangle$   
 584  $= 0.02$ , (b)  $\langle v'v' \rangle \in [0.0, 0.85]$  in steps  $\Delta\langle v'v' \rangle = 0.05$ , and (c)  $\langle u'v' \rangle \in [-0.2,$   
 585  $0.2]$  in steps  $\Delta\langle u'v' \rangle = 0.02$ . Solid (dotted) lines correspond to positive (negative)  
 586 contours. The black thick line delimits the recirculation bubble.

587 instead  $x_{\bar{u}}$  at locations perfectly compatible with experiments at  
 588 nearby Reynolds numbers,<sup>48</sup> although  $|\bar{u}_{\min}|$  seems to be a little  
 589 low. Centerline streamwise normal Reynolds stresses ( $\langle u'u' \rangle$ )  
 590 show the expected double-peak distribution, with the first peak

591 **TABLE III.** Peak values of flow field statistics along the wake centerline. Double-valued streamwise normal Reynold stress columns ( $\langle u'u' \rangle_{\max}$  and  $x_{\langle u'u' \rangle}$ ) denote double-peak  
592 or inflection plus peak distribution. Inflection points are given in parentheses.  
593

594 Author (references)	595 Case	596 $Re$	597 $\bar{u}_{\min}$	598 $x_{\bar{u}}$	599 $\langle u'u' \rangle_{\max}$	600 $x_{\langle u'u' \rangle}$	601 $\langle v'v' \rangle_{\max}$	602 $x_{\langle v'v' \rangle}$	603 $\langle w'w' \rangle_{\max}$	604 $x_{\langle w'w' \rangle}$
Present results	Case 1		-0.242	1.520	(0.084)/0.108	(1.466)/2.016	0.392	2.267	0.081	1.832
	Case 2		-0.266	1.580	(0.083)/0.108	(1.466)/2.027	0.401	2.245	0.083	1.867
	Case 3		-0.318	1.672	0.082/0.082	1.523/2.027	0.409	2.187	0.085	1.764
	Case 4		-0.302	1.718	0.086/0.087	1.504/2.004	0.373	2.245	0.093	1.764
Norberg <sup>48</sup>		1 500	-0.4	1.75	0.09/0.1024	1.51/2.23			0.1521	1.61
		3 000	-0.44	1.65	0.1089/0.1156	1.45/2.09			0.1296	2.08
		5 000	-0.45	1.42	0.1225/0.1296	1.23/1.83			0.1521	1.86
		8 000	-0.35	1.17	(0.1369)/0.2025	(1.02)/1.62			0.1521	1.41
		10 000	-0.38	1.04	(0.1369)/0.1849	(0.96)/1.50				
Konstantinidis <i>et al.</i> <sup>58</sup>		1 550			0.1089	2.1	0.2809	2.1		
		2 150			0.1024	2.1	0.2916	2.1		
		2 750			0.0961	2.1	0.3136	2.1		
		7 450			0.1225	1.5	0.4761	1.5		
Parnaudeau <i>et al.</i> <sup>49</sup>		3 900	-0.34	1.59	0.087	1.372				
Lourenco and Shih <sup>45</sup>		3 900	-0.24	0.72						
Beaudan and Moin <sup>50</sup>		3 900	-0.33	1.00						
Kravchenko and Moin <sup>54</sup>	$N_z = 48^F$	3 900	-0.37	1.4–1.5						

608 location and height in excellent agreement with experiments.<sup>48,58</sup>  
609 The location of the second peak is also within a reasonable distance  
610 of the experimental results, but the height appears slightly  
611 low. The same occurs with the single-peak location and value of  
612 crossflow ( $\langle v'v' \rangle$ ) and spanwise ( $\langle w'w' \rangle$ ) normal Reynolds stresses.  
613 The location is correctly predicted, but the peak height is somewhat  
614 off.

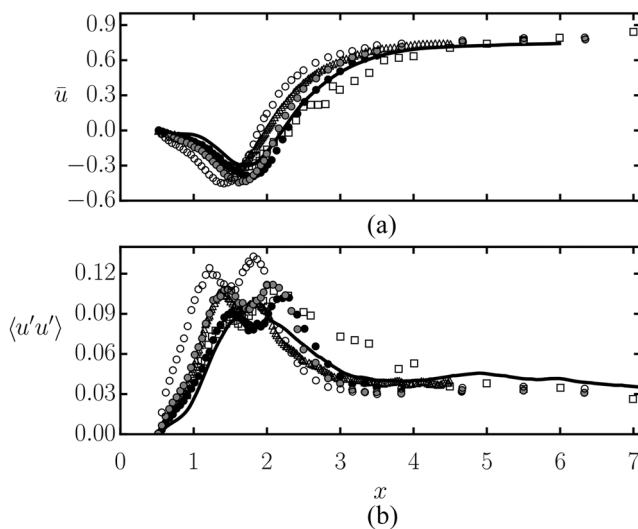
615 Absolute in-plane peak values for  $\langle u'u' \rangle$ ,  $\langle v'v' \rangle$ , and  $\langle w'w' \rangle$ ,  
616 reported in Table IV, are in reasonably good agreement with the  
617 experiments by Konstantinidis *et al.*<sup>59,60</sup>

618 Figure 5(a) shows the mean streamwise velocity distribution  
619 along the wake centerline  $\bar{u}(x, 0)$ . Starting from rest at the cylinder  
620 base (corresponding to  $x = x_b = 0.5$ ),  $\bar{u}$  initially decreases into

621 negative, reaches a minimum at about  $x \sim 1.5$ , and then quickly  
622 recovers in the near-wake, leaving a velocity deficit of around  
623  $1 - \bar{u}(x, 0) \sim 0.3$  that is very slowly further recovered in the mid- and  
624 far wakes. The region where  $\bar{u}(x, 0) < 0$  delimits the streamwise  
625 extent of the mean recirculation bubble such that the recirculation  
626 bubble length  $L_r$  is obtained from  $\bar{u}(x_b + L_r, 0) = 0$ . This  
627 is not to be confused with wake formation length, defined as  
628  $L_f \equiv \text{argmax}_x[\langle u'u' \rangle(x, 0)] - x_b$ . Our numerical results (case 3) follow  
629 a trend that is fully compatible with the experiments by Norberg,<sup>48</sup>  
630 except that their minima seem to reach fairly lower values  
631 (see Table III). The location of the minimum for our  $Re = 2000$  computation  
632 occurs precisely within the range set by the experiments at  
633  $Re = 1500$  and  $3000$ . The experiment by Konstantinidis *et al.*<sup>58</sup> at  
634  
635  
636  
637  
638  
639  
640  
641  
642  
643  
644  
645

620 **TABLE IV.** Peak values of off-centerline near-wake flow field statistics.  
621

622 Author (references)	623 Case	624 $Re$	625 $\bar{u}_{\min}$	626 $x_{\bar{u}}$	627 $\langle u'u' \rangle_{\max}$	628 $x_{\langle u'u' \rangle}$	629 $\langle v'v' \rangle_{\max}$	630 $x_{\langle v'v' \rangle}$	631 $\langle u'v' \rangle_{\max}$	632 $x_{\langle u'v' \rangle}$	633 $\langle w'w' \rangle_{\max}$	634 $x_{\langle w'w' \rangle}$
Present results	Case 1	2000			0.211	1.691	0.392	2.267	-0.106	2.112	0.081	1.832
	Case 2				0.206	1.751	0.401	2.245	0.108	2.146	0.083	1.867
	Case 3				0.180	1.736	0.409	2.187	0.1059	2.269	0.085	1.764
	Case 4				0.177	1.803	0.373	2.245	0.111	2.215	0.093	1.764
Konstantinidis <i>et al.</i> <sup>59</sup>		2160			0.15		0.32		0.09			
Konstantinidis and Balabani <sup>60</sup>		2150			0.16		0.33		0.09			
Parnaudeau <i>et al.</i> <sup>49</sup>					0.114	??						
Dong <i>et al.</i> <sup>61</sup>	PIV	4000	-0.252	1.5	0.2025	1.55			0.11	2.05		
	DNS	3900	-0.291	1.35	0.1806	1.72			0.14	1.90		
Lehmkuhl <i>et al.</i> <sup>56</sup>	Mean	3900	-0.261	1.396	0.237	1.576	0.468	2.00	-0.125	1.941		
	L		-0.323	1.590	0.223	1.723	0.441	2.105	-0.126	2.107		
	H		-0.233	1.334	0.270	1.489	0.520	1.922	-0.136	1.941		



646 **FIG. 5.** Recirculating region characteristics along the wake centerline: (a) mean  
 647 streamwise velocity ( $\bar{u}$ ) profile and (b) Reynolds streamwise normal stress ( $\langle u'u' \rangle$ )  
 648 profile along the wake centerline. Shown are case 3 (solid line); experiments by  
 649 Norberg<sup>48</sup> (circles: full black:  $Re = 1500$ , dark gray:  $Re = 3000$ , empty:  $Re = 5000$ ),  
 650 Konstantinidis *et al.*<sup>58</sup> (squares: 2150) and Parnaudeau *et al.*<sup>49</sup> (triangles:  $Re =$   
 3900).

651  $Re = 2150$ , instead, features minima very close to our numerical  
 652 results, although the data display significant scatter and the velocity  
 653 defect recovery appears unusually slow. It must be borne in  
 654 mind that preturbulence levels were particularly high in these exper-  
 655 iments. The experiment by Parnaudeau *et al.*<sup>49</sup> at  $Re = 3900$  shows  
 656 also minimum  $\bar{u}(x, 0)$  and a recovery rate similar to those in our  
 657 numerics, while at the same time, the minimum is located halfway  
 658 between the minima of Norberg<sup>48</sup> for  $Re = 3000$  and 5000.

659 The comparison of the streamwise distribution of the  
 660 streamwise velocity fluctuation autocorrelation [streamwise nor-  
 661 mal Reynolds stress  $\langle u'u' \rangle(x, 0)$ ] along the wake centerline, shown  
 662 in Fig. 5(b), is somewhat less straightforward. While Norberg<sup>48</sup>  
 663 reported two-peak distributions, typical of U-type wake states, that  
 664 shift to lower  $x$  and higher maxima as  $Re$  is increased, Konstantinidis  
 665 *et al.*<sup>58</sup> presents the inflection plus peak distribution that is char-  
 666 acteristic of V-type states. The recovery tails of the latter are also  
 667 longer, possibly due to high preturbulence levels. The distal peak in  
 668 the double-peak distributions of Norberg<sup>48</sup> is higher than the prox-  
 669 imal peak, the dissymmetry being larger at the lowest  $Re = 1500$ .  
 670 Parnaudeau *et al.*<sup>49</sup> also observed a double-peak distribution at  
 671  $Re = 3900$ , but the first peak rises slightly above the second in this  
 672 case. The  $\langle u'u' \rangle(x, 0)$  distribution in our numerical simulations on  
 673 the two largest spanwise domains employed (cases 3 and 4) seems  
 674 closer to that of Parnaudeau *et al.*<sup>49</sup> than that of Norberg<sup>48</sup> or Kon-  
 675 stantinidis *et al.*,<sup>58</sup> even though the latter explored Reynolds num-  
 676 bers closer to ours. When shorter spanwise domains are used, how-  
 677 ever, the distributions tend to the inflection plus peak characteristic  
 678 shape. This is in overt contradiction with prior observations that the  
 679 U-type state is favored by smaller spanwise domains. The issue  
 680 remains unexplained.

681 The agreement with experiments is fair in the mid-wake  
 682 and beyond as cross-stream profiles of velocity components and  
 683 Reynolds stresses at various locations  $x \geq 3$  confirm (not shown).  
 684 Computationally obtained profiles overlap reasonably with experi-  
 685 mentally measured<sup>47,59</sup> and numerically computed<sup>50,53,64,69</sup> distribu-  
 686 tions.

687 The categorization of the near-wake state into U- or V-type  
 688 is based on the cross-stream profile of streamwise velocity at a  
 689 precise streamwise location:  $\bar{u}(1, y)$ . As already stated in Sec. I,  
 690 every shape ranging from a clear-cut U to a sharp V has been  
 691 reported in the literature. Figure 5 points at a gradual evolution  
 692 of wake statistics as  $Re$  is increased but at the same time unveils  
 693 high sensitivity to experimental conditions. While the size of the  
 694 recirculation bubble in the near wake seems to evolve smoothly  
 695 with  $Re$  for a given experimental setup, different experiments report  
 696 dissimilar bubble sizes at the same exact  $Re$  such that compar-  
 697 ing cross-stream velocity distributions at a fixed location is at  
 698 the very least deceptive. The effect of experimental conditions or  
 699 numerical details can, to a great extent, be accounted for with an  
 700 offset in  $Re$ . Comparison at a location defined in relative terms  
 701 appears thus as a much sounder approach. The results compared  
 702 in this way cannot be expected to match exactly since not only  
 703 the size but also the topology of the recirculation bubble evolves  
 704 with  $Re$ . Accordingly, the transformation from one experiment and  
 705 Reynolds number to another can only partially be explained in  
 706 terms of a mere streamwise scaling or shift. We choose here to  
 707 scale the  $x$  coordinate to align the location  $x_{\bar{u}}$  of the minimum  $\bar{u}_{\min}$   
 708 of  $\bar{u}$ .

709 Figure 6 shows cross-stream velocity profiles of streamwise ( $\bar{u}$ )  
 710 and cross-stream ( $\bar{v}$ ) velocities at  $x = 1, 1.5, 2$  for Ref. 48 and Ref.  
 711 59 and at nearby locations  $x = 1.06, 1.54, 2.02$  for Ref. 49. Statisti-  
 712 cally averaged profiles are expected to be reflection-symmetric with  
 713 respect to the wake centerline:  $[\bar{u}, \bar{v}](x, y) = [\bar{u}, -\bar{v}](x, -y)$ . Fail-  
 714 ure to preserve this symmetry would indicate lack of symmetry in  
 715 the experiment (or in the measurement probe locations) or, alterna-  
 716 tively, poorly converged statistics due to insufficient data. In this  
 717 sense, the degree to which the symmetry is accomplished acts as a  
 718 metric for the quality of the results. Although the degree of asym-  
 719 metry in the raw simulation data was already small, we have chosen  
 720 here to symmetrize numerically obtained profiles as a means of dou-  
 721 bling the data sample size. The cross-stream profiles of streamwise  
 722 velocity  $\bar{u}$  evolve from a U shape very close to the cylinder base  
 723 ( $x \approx 1$ ) toward a V shape as we move backward within the near-  
 724 wake ( $x \approx 2$ ). This alone illustrates how U- or V-shaped profiles  
 725 can be obtained at will by adequately shifting the sampling loca-  
 726 tion. Wakes that are topologically identical but have slightly different  
 727 recirculation bubble lengths will produce very different results if the  
 728 same location is chosen for comparison. As a matter of fact, our  
 729 raw data feature slightly flatter profiles at  $x = 1$  and  $x = 1.5$  and  
 730 somewhat lower velocities at  $x = 2$  when compared with those of  
 731 Parnaudeau *et al.*<sup>49</sup> When sampling locations are corrected for cir-  
 732 culation bubble size, the agreement is remarkable despite the signifi-  
 733 cant disparity in Reynolds number ( $Re = 2000$  here against  $Re = 3900$   
 734 for the experimental data). Remaining discrepancies can be safely  
 735 ascribed to this fact and also to mild experimental inaccuracies, as  
 736 evidenced by a slight asymmetry in the profiles. Something similar  
 737 occurs when analyzing cross-stream velocity profiles  $\bar{v}$  in Fig. 6(b).  
 The significant deviations observed at  $x = 1$  and 1.5, with much

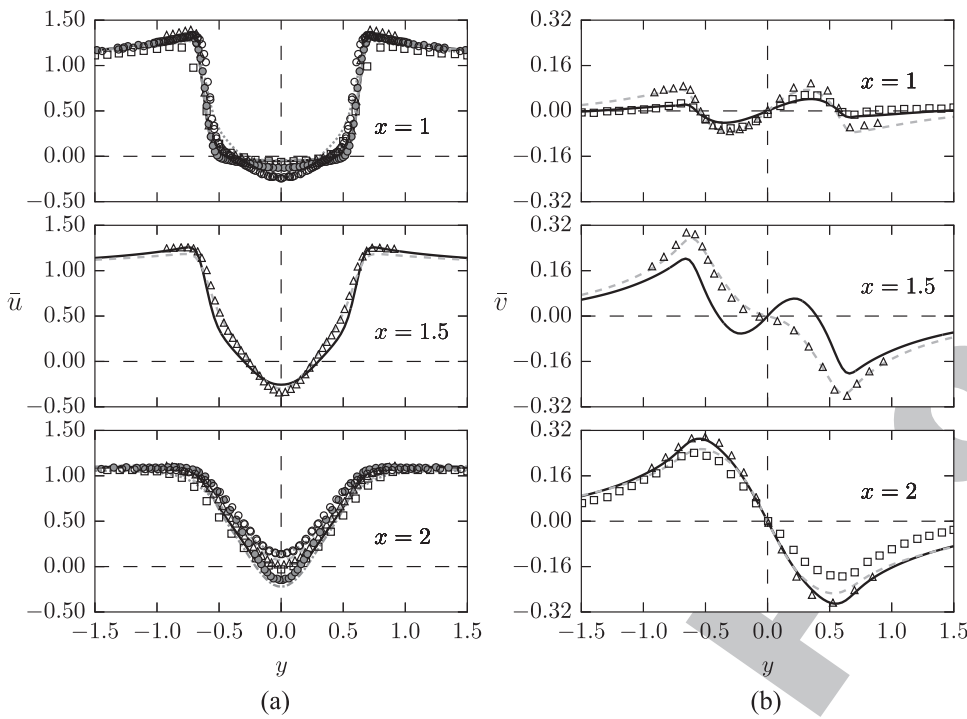


**FIG. 6.** Cross-stream profiles of mean (a) streamwise  $\bar{u}$  and (b) cross-stream  $\bar{v}$  velocities in the near wake. Sampling locations are  $x = 1$  (top),  $x = 1.5$  (middle), and  $x = 2$  (bottom). Shown are case 3 (solid line); experimental results by Konstantinidis *et al.*<sup>59</sup> (squares,  $Re = 2160$ ), Norberg<sup>48</sup> (dark gray circles:  $Re = 3000, 3500$ ; open circles:  $Re = 5000$ ), and Parnaudeau *et al.*<sup>49</sup> (triangles,  $Re = 3900$ , at nearby locations  $x = 1.06, 1.54, \text{ and } 2.02$ ); numerical results corrected for Norberg<sup>48</sup> (gray dashed-dotted line,  $Re = 3000, 3500$ ; gray dotted line  $Re = 5000$ ) and for Parnaudeau *et al.*<sup>49</sup> (gray dashed line).

743  
744  
745  
746  
747  
748  
749  
750  
751  
752  
753  
754  
755  
756  
757  
758

738 flatter profiles, are fully resolved upon correction. At  $x = 2$ , the agree-  
739 ment was already good prior to correction and scaling weakens the  
740 agreement. The different wake topologies are to be held responsible for this.

Taking Ref. 48 as a baseline for comparison, bubble length correc-  
741 tion of simulation results yields fairly good recovery of  $\bar{u}$  profiles  
742 at both  $Re = 3000$  and  $5000$ , while no experimental data are avail-  
743 able for  $\bar{v}$ . Finally, the numerical bubble size is sufficiently close to  
744

759  
760  
761  
762

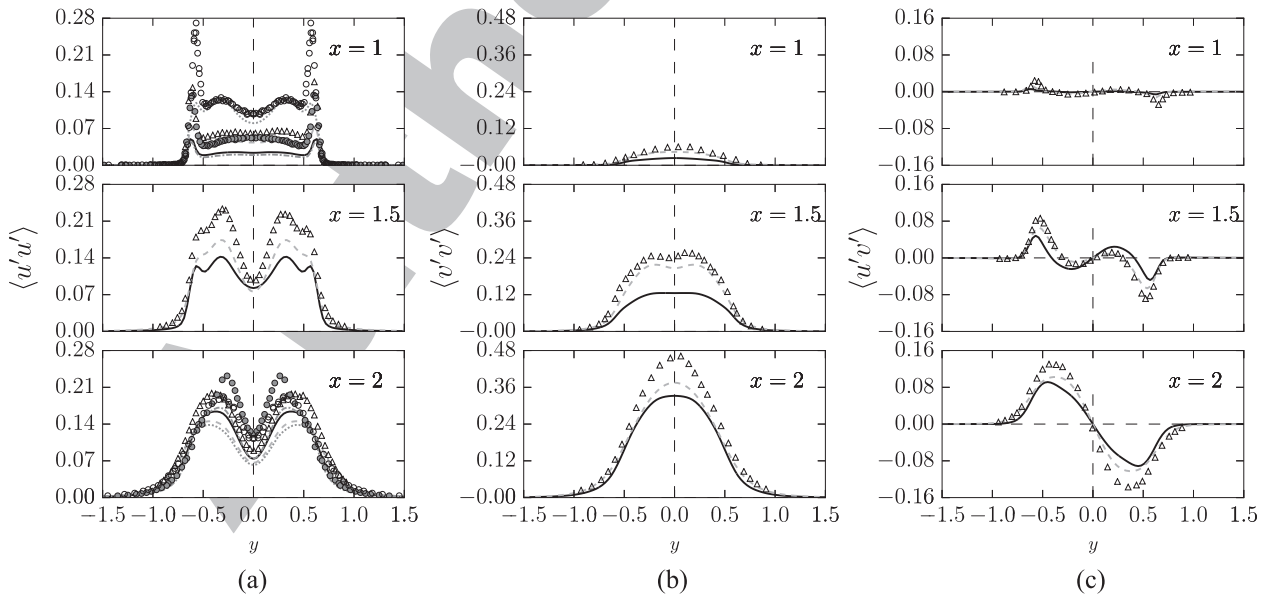


**FIG. 7.** Cross-stream profiles of Reynolds stresses (second-order moments) in the near wake. (a) Streamwise  $\langle u'u' \rangle$  and (b) cross-stream  $\langle v'v' \rangle$  velocity fluctuation self-correlations. (c) Streamwise-cross-stream velocity fluctuation cross correlations  $\langle u'v' \rangle$ . Styles and symbols as in Fig. 6.

741  
742

that obtained at  $Re = 2160$  by Konstantinidis *et al.*<sup>59</sup> so that the correction to be applied is almost imperceptible. The agreement is fair at all locations for  $\bar{u}$  and all but  $x = 2$  for  $\bar{v}$ , where the experiments produced a slightly flatter profile than observed in the numerics.

Cross-stream profiles of second-order moments, i.e., Reynolds stresses, are shown in Fig. 7. Streamwise velocity fluctuation self-correlations  $\langle u'u' \rangle$  display the double-peak shape (with nearly fluctuation-free wake core) at  $x = 1$  that is characteristic of the U-type wake state. Two distinct phenomena are responsible for these peaks, which are located on the top and bottom boundaries of the recirculation bubble. On the one hand, the shear layers resulting from boundary layer detachment at either side of the cylinder flap synchronously due to the von Kármán instability and the associated shedding of alternate counter-rotating vortices. On the other hand, these same shear layers are subject to turbulent transition, with the ensuing occurrence of turbulent fluctuations. As we progress downstream within the near-wake, the amplitude increase of the shear layer flapping results in the diffusion of Reynolds stresses such that the peaks broaden and drift toward the wake centerline as fluctuations gradually penetrate the recirculation bubble core. The  $\langle u'u' \rangle$  profile shape compares favorably with the experiments by Parnaudeau *et al.*,<sup>49</sup> but the levels are significantly lower for the numerical data, particularly so in the very near-wake. Correction for recirculation bubble size acts in the right direction by lifting the plateau around the wake centerline to comparable levels, but peak values remain low. Contrasting with the experimental data by Norberg<sup>48</sup> at  $Re = 3000$  ( $x = 1$ ) and  $Re = 3500$  ( $x = 2$ ), the numerics also qualitatively capture the right functional shape but quantitatively fall short of experimental values. In this case, correction does not improve the situation as the minimum of  $\bar{u}$  for numerics and experiments is already aligned and the scaling factor is very close to unity. Nonetheless, while it is not surprising that turbulent fluctuation levels are higher at the higher  $Re$  at which the experiments were done, the outline of the profiles is properly captured by the numerics. The exact same reasoning applies to cross-stream velocity self-correlations [Fig. 7(b)] and streamwise-cross-stream cross correlations [depicted in Fig. 7(c)], for which only the experimental data of Parnaudeau *et al.*<sup>49</sup> are available. Once again, qualitative agreement is excellent, while quantitative match is improved by correction but remains elusive. There is a reasonable explanation to the level mismatch in second-order statistics. Peak values of Reynolds stresses occur within the shear layers developing at either side of the cylinder, and turbulence levels in this region are naturally dependent on shear layer thickness, which in turn scales with the Reynolds number. Quantitative agreement is therefore not to be expected.

## IV. DISCUSSION

### A. Shear layer instability

Planar steady shear layers may be subject to the Kelvin–Helmholtz instability. In the case of the transitional flow past a cylinder, the shear layers resulting from boundary layer separation are neither planar nor steady. The Kármán instability induces a flapping motion of the wake, and a secondary instability of the von Kármán street introduces a spanwise modulation that propagates upstream in the wake and reaches, to some degree, the immediate

vicinity of the cylinder. Notwithstanding this, shear layer instability has been observed in the cylinder near wake. The precise critical value  $Re_{KH}$  (or  $Re_{SL}$ ) for the inception of the Kelvin–Helmholtz (or shear layer) instability is largely dependent on extrinsic factors such as end boundary conditions, background disturbance intensity, and preturbulence levels.<sup>28</sup> For an experimental setup favoring parallel shedding conditions, the instability might occur as early as  $Re_{KH} = 1200$ , while oblique shedding pushes the shear layer instability to  $Re_{KH} = 2600$ . The instability, when present, emerges as a spatially developing train of small scale vortices characterized by velocity fluctuations of a frequency that is substantially higher than that of Kármán vortices. Kelvin–Helmholtz vortices are continuously being generated early on in the shear layer and grow as they are advected downstream. When they reach the Kármán vortex formation region, a number of them accumulate, coalesce, and are swallowed into the forming wake vortex. Using theoretical scaling arguments for the separating boundary layer on the cylinder walls and the ensuing shear layers to fit experimental data from several sources, Prasad and Williamson<sup>33</sup> suggested a power law  $f_{KH}/f_{vK} = 0.0235Re^{0.67}$ , relating the shear layer  $f_{SL} \equiv f_{KH}$  and von Kármán  $f_{vK}$  shedding frequencies.

A velocity probe strategically located in the shear layer at  $(x, y, z) = (0.8, 0.6, 1.25)$  clearly detects the flapping motion of the wake for most of the time, as shown by the low-frequency-low-amplitude oscillation of the cross-stream velocity  $v$  in the inset of Fig. 8. The signal, however, experiences occasional sudden bursts of much higher frequency and amplitude. Averaging the individual spectra of 64 velocity signals measured for a time lapse in excess of 20–25 vortex shedding cycles along a probe array at  $(x, y) = (0.8, 0.6)$  results in the average spectrum shown in Fig. 8. Alongside the distinct vortex shedding fundamental frequency  $f_{vK}$  and its first harmonic, a broad-band low amplitude peak  $f_{KH}$  is discernible. This peak corresponds to the shear layer instability, and although the associated velocity fluctuations are large, its moderate amplitude results from the phenomenon occurring only occasionally. The peak is located at  $f_{KH} \approx 3.902f_{vK}$ , which falls right on top of the power law advanced by Prasad and Williamson.<sup>23</sup>

In order to suppress the von Kármán-related oscillation from the probe array readings and thus isolate the shear layer oscillation, the signals have been processed with a high-pass fifth-order

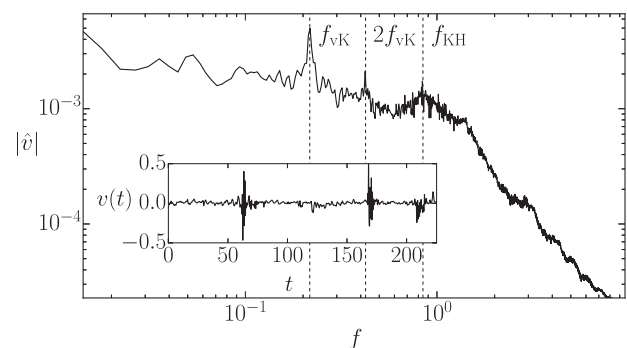
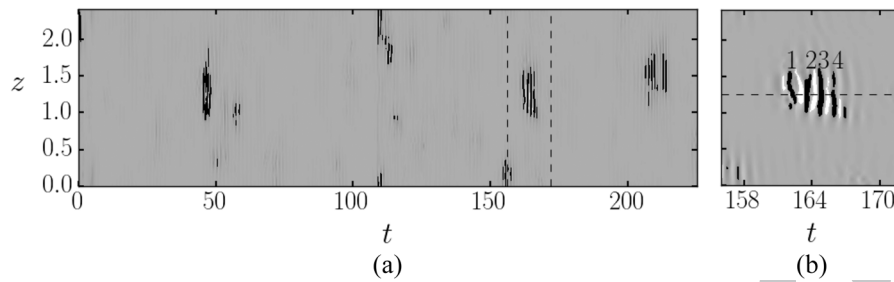


FIG. 8. Average spectrum of the crossflow velocity signals along a probe array located in the shear layer at  $(x, y) = (0.8, 0.6)$ . The inset shows one such signal for the probe at  $(x, y, z) = (0.8, 0.6, 1.25)$ .



**FIG. 9.** Space–time diagram of filtered crossflow velocity  $v$  at  $(x, y)=(0.8, 0.6)$ . (a) Full time series. (b) Detail of the interval  $t \in [158, 172]$  [indicated with dashed lines in panel (a)] showing the passage of Kelvin–Helmholtz vortices. The horizontal and vertical dashed lines indicate the  $(z, t)$  coordinates drawn in Fig. 10. Labels 1, 2, 3, and 4 indicate stripes that correspond to consecutive shear-layer vortices traversing the location of the probe array.

861  
862  
863

864 Butterworth filter with cutoff frequency  $f_c = 0.7$ . The filtered sig-  
865 nals are displayed as space–time diagrams in Fig. 9. While there are  
866 no traces of the von Kármán frequency, which has been effectively  
867 filtered, occasional velocity oscillations are clearly observed as rip-  
868 ples that are elongated, albeit localized, in the spanwise direction.  
869 Very low amplitude ripples are perceptible here and there, but only  
870 a few grow to remarkably high amplitude. These oscillations are con-  
871 sistent with the passage of small spanwise vortices resulting from  
872 a Kelvin–Helmholtz instability of the shear layer, but the incipient  
873 three-dimensionality of the flapping shear layer restrains their  
874 spanwise extent, which remains always well below  $1D$ . This does  
875 not preclude that, at higher Reynolds, shear layer vortices become  
876 more elongated in the spanwise direction, thus preserving better  
877 two-dimensionality, as observed by Prasad and Williamson.<sup>23</sup> The  
878 intensification of the Kelvin–Helmholtz instability renders it per-  
879 ceptible further upstream on the shear layers, out of reach of the  
880 wake three-dimensionalization occurring downstream. The inter-  
881 mittency factor at the probe location, defined as the fraction of the  
882 time that high frequency oscillations are present, is  $\gamma \simeq 6$ , although  
883 much longer time series would be required to obtain converged  
884 values.

884 Figure 10 depicts cross-sectional streamlines at  $z = 1.25$  of the  
885 instantaneous velocity field at  $t = 165.7$ , showing four consecutive  
886 shear-layer vortices duly numbered and labeled in Fig. 9. Vortices 1,  
887 2, and 3 have already traversed the sampling probe location (cross  
888 sign), while vortex 4 is headed toward it.

889 **B. Secondary instability of Kármán vortices**

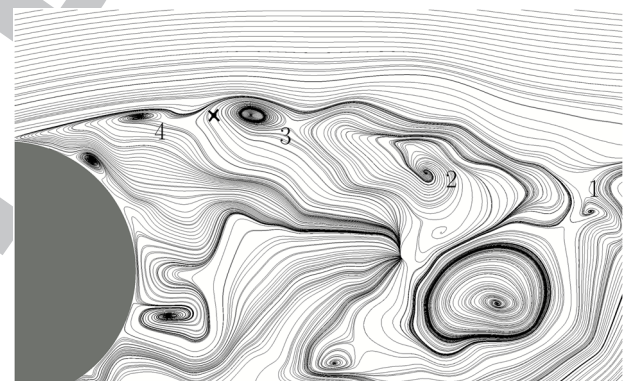
890 The cylinder wake is three-dimensional from Reynolds num-  
891 bers as low as  $Re \lesssim 190$ <sup>16</sup> following well established secondary in-  
892 stabilities of von Kármán vortices.<sup>10,17</sup> Here, we are interested in the  
893 remnants of these instabilities at a much higher Reynolds number  
894  $Re = 2000$ , for which von Kármán vortices remain the dominant  
895 structure in the wake but are perturbed by spanwise modulation and  
896 superimposed spatiotemporal turbulent fluctuations.

897 In order to analyze the three-dimensional nature of the flow,  
898 we have followed Mansy *et al.*<sup>33</sup> in decomposing the flow field in a  
899 primary [two-dimensional,  $\mathbf{u}_2(\mathbf{r}_2; t) = \bar{\mathbf{u}}(\mathbf{r}_2) + \mathbf{u}'_2(\mathbf{r}_2; t)$ ] and a sec-  
900 ondary [three-dimensional,  $\mathbf{u}_3(\mathbf{r}; t)$ ] component. In the restricted  
901 spanwise extent of the computational domains employed, there  
902 is no room for the development of oblique shedding or vortex

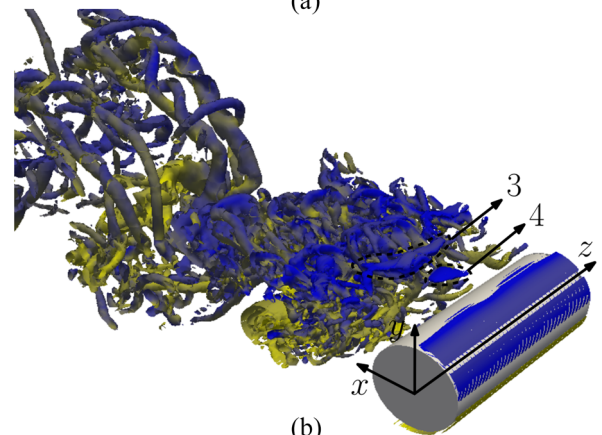
903 dislocation such that this decomposition does indeed properly sepa-  
904 rate all three-dimensional effects from primary vortex shedding.

905 Figure 41(a) shows the spacetime diagram of streamwise veloc-  
906 ity  $u$  for a probe array located beyond the vortex formation region

903  
904  
905  
906



(a)



(b)

**FIG. 10.** Kelvin–Helmholtz instability in the shear-layer. (a) Streamlines of the instantaneous velocity field at  $z = 1.25$  and  $t = 165.7$ , as indicated in Fig. 9. The cross indicates the location of the probe. The labels indicate consecutive shear-layer vortices. (b) Visualization of shear-layer vortices using the Q-criterion with value 5; coloring by spanwise vorticity  $w_z \in [-10, 10]$ .

907  
908  
909  
910  
911

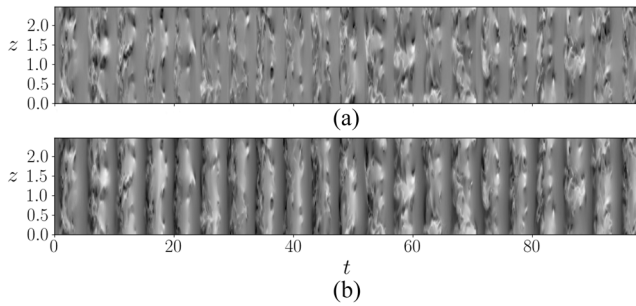


FIG. 11. Spacetime diagrams of streamwise velocity at  $(x, y) = (3, 0.5)$  for (a) the total (primary and secondary combined)  $u = u_2 + u_3$  and (b) the secondary flow  $u_3$ .

912  
913

914 at  $(x, y) = (3, 0.5)$ . A vertical-banded pattern, associated with vortex shedding, is clearly distinguishable. The effect of subtracting the primary flow from the total flow, yielding the secondary flow in isolation, is shown in Fig. 11(b). It is clear from the alternate homogeneous and inhomogeneous stripes that three-dimensionality is concentrated at certain phases along the vortex shedding cycle.

920 The spectra of the total, primary  $u_2$ , and rms secondary  $u_3^{\text{rms}} \equiv \sqrt{\langle u_3^2 \rangle_z}$  streamwise velocity signals are shown in Fig. 12(a). As expected, the primary signal has a clear peak at the Strouhal frequency, and two higher harmonics are also discernible. The secondary signal is somewhat flatter, but protrusions at the Strouhal frequency and a couple of harmonics are still visible, which indicates that the signals are coupled. The cross-spectral-density  $S_{23}$  of the primary and secondary signals is shown in Figs. 12(b) and 12(c) to analyze the cross correlation or coherence between the signals. There is a clear peak of the cross-spectral-density modulus ( $A_{23} \equiv |S_{23}|$ , top panel) at precisely the Kármán frequency, indicating that the energy contents at this frequency of both signals are correlated. The cross-spectral-density phase [ $\varphi_{23} \equiv \arg(S_{23})$ ] reveals an associated phase lag  $\varphi_{23}(f_{\text{vK}}) \approx 225^\circ$ . Since the primary signal peaks upon the crossing of the Kármán vortex through the sampling location, the detected phase lag implies that three-dimensionality is maximum in the trailing portion of the braid region that connects counter-rotating consecutive vortices.

938 Figure 13 illustrates the location of maximum three-dimensionality with two snapshots of the spanwise vorticity field that are apart by exactly  $\varphi_{23}(f_{\text{vK}})$  along one vortex shedding cycle. The first one corresponds to a maximum of the primary signal as recorded at the sampling location (cross), which is being traversed by a Kármán vortex. The second one, taken  $\varphi_{23}(f_{\text{vK}})$  later, shows that the sampling location is right at the braid region in between consecutive vortices. This is consistent with the short-wavelength mode B observed in the cylinder wake at much lower Reynolds numbers, as the instability leading to it is known to nucleate at the braid shear layers,<sup>10,75</sup> while Mode A results from the instability of the vortex core regions. Strong counter-rotating streamwise vortex pairs can be detected in the braid regions every now and then, but the spanwise periodic pattern of mode B has long been disrupted such that vortices appear in isolation or with irregular spacing at best. The streamwise coherence of mode B streamwise vortices at onset, which

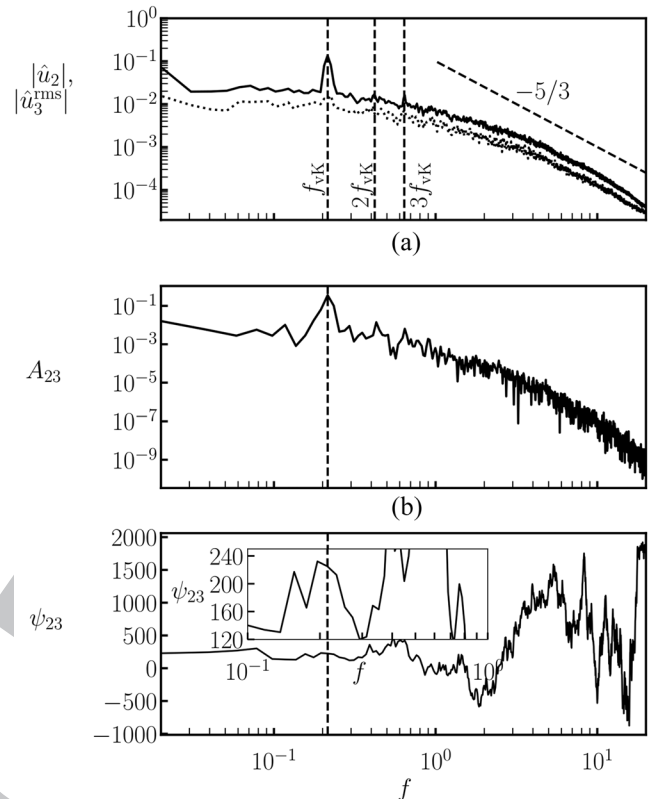


FIG. 12. Spectra of the total ( $u$ , black), primary ( $u_2$ , dark gray), and rms secondary ( $u_3^{\text{rms}}$ , light gray) flow components of the streamwise velocity signal at  $(x, y) = (3, 0.5)$ . (b) Cross-spectral-density  $S_{23}$  of the primary  $u_2$  and secondary  $u_3^{\text{rms}}$  signal pair [top: cross-modulus  $A_{23} \equiv |S_{23}|$ , bottom: cross-phase  $\varphi_{23} = \arg(S_{23})$ ].

954  
955  
956  
957

958 accounted for a characteristic symmetry from one braid to the next of opposite sign, is lost once turbulence sets in. Two-dimensional (time and  $z$ -coordinate) cross correlation of  $u_3$  signals taken along probe arrays at  $(x, y) = (3, 0.5)$  and  $(x, y) = (3, -0.5)$  fail to produce the clear peak one would expect for space-time drifts  $(\zeta, \tau) = (0, \pi/f_{\text{vK}})$  if mode B symmetry was preserved. The effect of turbulent transition is that of decorrelating any two signals separated by relatively short time or streamwise distance.

958  
959  
960  
961  
962  
963  
964  
965

### C. Spanwise length scale of large coherent three-dimensional structures

966  
967

968 Quantification of the spanwise length scale of the large coherent three-dimensional structures that are present in the wake requires monitorization of some quantity along spanwise lines. Particularly useful are signals that cancel out exactly for two-dimensional vortex-shedding as their mere deviation from zero is a sign of three-dimensionality. Fourier spectral differentiation has been employed along spanwise probe arrays to compute  $\tilde{\omega}_y = \frac{\partial u}{\partial z}$ , as an indicator of cross-stream vorticity. The usual approach of computing spanwise self-correlation or performing Fourier analysis works fine for spanwise(-pseudo)-periodic flow structures but fails whenever the

968  
969  
970  
971  
972  
973  
974  
975  
976  
977

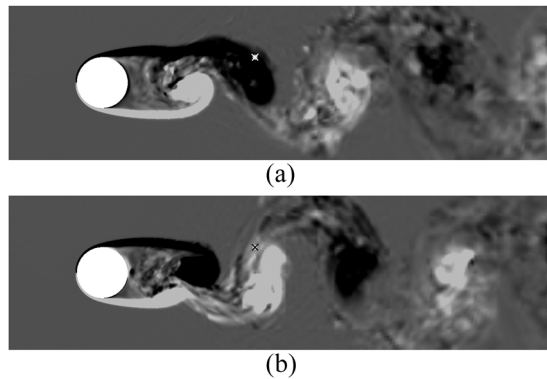


**FIG. 13.** Instantaneous spanwise vorticity  $\omega_z$  field snapshots at (a) a maximum of the primary signal  $u_2$  as measured by the sampling probe at  $(x, y) = (3, 0.5)$  and (b) a phase  $\varphi_{23}(f_{vK}) = 225^\circ$  later corresponding to a maximum of the secondary signal  $u_3^{\text{rms}}$ .

structures appear in isolation or show some localization features. The reason is that self-correlation and Fourier transforms act globally on the signal and provide global information such that structure spacing rather than size can be detected. A powerful tool for analyzing the local spectral features of a signal is the Hilbert transform. Spectrograms, wavelet transforms, and the Hilbert–Huang transform are alternative means, but the simplicity and versatility of the Hilbert transform make it more suitable for the analysis of spanwise length scales in the cylinder wake.<sup>38</sup> The Hilbert transform of a real-valued function  $f(z)$  is defined by its convolution with  $1/(\pi z)$  as

$$\mathcal{H}[f(z)] = \frac{1}{\pi} \int_{-\infty}^{\infty} \frac{f(\zeta)}{z - \zeta} d\zeta,$$

where the improper integral must be understood in the Cauchy principal value sense. The complex-valued function  $f_a(z) = f(z) + i\mathcal{H}[f(z)]$  is the analytic representation of  $f(z)$ , and its modulus and argument, advisedly named local (instantaneous if the independent variable is time) amplitude and phase, respectively, provide insight into the local (instantaneous) properties of the original signal.

Thus, the analytic signal  $\tilde{\omega}_y^a(z, t)$  is obtained from  $\tilde{\omega}_y(z, t)$  and  $\mathcal{H}_{\tilde{\omega}_y}(z, t)$  as the complex function,

$$\omega(z, t) \equiv \tilde{\omega}_y^a(z, t) = \tilde{\omega}_y(z, t) + i\mathcal{H}_{\tilde{\omega}_y}(z, t) = A_\omega(z, t)e^{i\varphi_\omega(z, t)}.$$

Its modulus  $A_\omega \equiv |\omega|$  and argument  $\varphi_\omega \equiv \arg(\omega)$  contain information on the local amplitude (envelope) and phase, respectively, of  $\tilde{\omega}_y$ . The instantaneous local spanwise wavelength of the signal is then recovered from

$$\frac{2\pi}{\lambda_z(z, t)} = \frac{d\varphi_\omega}{dz}.$$

The probability density function (PDF) of  $\lambda_z$  has been computed via Normal/Gaussian kernel density estimation with a bandwidth  $\Delta z = 0.04$  and scaled by the mean instantaneous envelope  $\langle A_\omega \rangle_z(t)$  so as to account for the energy level contained in the most predominant three-dimensional structures.

Figure 14 presents the time evolution of the  $\langle A_\omega \rangle_z$ -scaled  $\lambda_z$ -PDF instantaneous distributions as processed from the readings obtained using the probe array located at  $(x, y) = (3, 0.5)$ . The shading denotes the instantaneous probability distribution of  $\lambda_z$ , with darker regions corresponding to the most recurrent length scales of energetic spanwise structures. Long wavelength structures are rare, as evidenced by the predominance of white for large  $\lambda_z$ . Meanwhile, shaded regions appear for relatively low  $\lambda_z$  in the form of time-localized spots with a certain (pseudo-)periodicity. Energetic spanwise structures occur intermittently, with characteristic frequency (that of vortex shedding) and spanwise size distribution. The  $C_L$  signal has been superimposed to the colormap to illustrate the existing correlation between the occurrence of spanwise flow structures and the vortex shedding process. As already anticipated by the secondary flow spacetime diagram of Fig. 11, three-dimensionality occurs predominantly at certain phases of the vortex-shedding cycle, which translates into precise streamwise locations along the vortex street, namely, the braid regions in between opposite sign vortices.

The  $C_L$  signal has been used to uniquely define a phase along the vortex-shedding cycle. The Hilbert transform has been used again, this time to turn  $C_L$  into an analytical time signal  $C_L^a(t) = C_L(t) + i\mathcal{H}_{C_L}(t)$  such that the phase can be obtained as  $\theta(t) \equiv \arg(C_L^a(t))$ . The right panel of Fig. 14 zooms into a full vortex-shedding cycle and indicates eight equispaced phases  $\theta_i = 2\pi i/8$  ( $i \in [0, 7]$ ) along it. Four distinct stages can be clearly

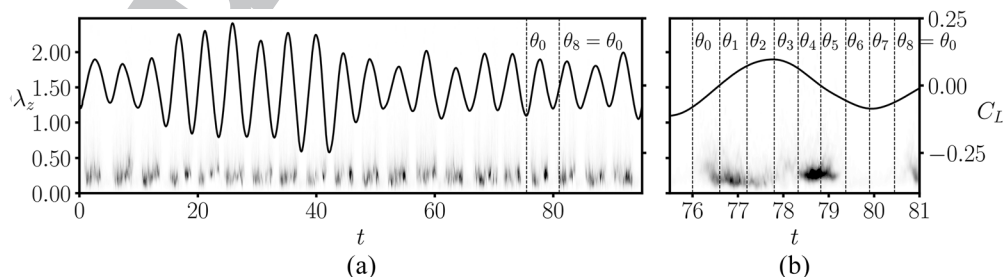


**FIG. 14.** Time evolution of the lift coefficient  $C_L$  (right axis) and PDF of the instantaneous spanwise wavelength  $\lambda_z$  distribution at  $(x, y) = (3, 0.5)$ , scaled by the mean instantaneous envelope  $\langle A_\omega \rangle_z$  (left axis). (a) Full time-series. (b) Detail of  $t \in [75, 82]$ . The vertical dashed lines indicate the time instants for eight equispaced  $C_L$  signal phases  $\theta_i = 2\pi i/8$  ( $i \in [0, 7]$ ).

identified during the cycle. For around one quarter of the cycle, represented by phases  $\theta_6$  through  $\theta_8 = \theta_0$ , the wake has no perceptible three-dimensionality at the sampling location. Later on, three-dimensional spanwise structures of very small size start being observed at the probe array with increasing probability that peaks between phases  $\theta_1$  and  $\theta_2$ . Beyond this first probability peak, the recurrence of the structures declines to some extent, reaching a local minimum in between phases  $\theta_3$  and  $\theta_4$ . Past this stage, spanwise structures regain presence and their probability of occurrence reaches a second peak at phase  $\theta_5$ . The spanwise extent of the three-dimensional structures progressively grows as their recurrence declines from the first probability peak and bounces back toward the second peak. The most probable structures are therefore slightly larger, although still rather small, for the second peak than for the first. Beyond the second peak, three-dimensionality quickly vanishes before the cycle starts anew.

In order to substantiate the cyclic nature of the spanwise flow structures measured at a fixed  $(x, y)$ -location in the wake, phase averaging of the flow field has been undertaken. The data comprised in the interval  $\theta \in [\theta_i - \pi/8, \theta_i + \pi/8]$  ( $i \in [0, 7]$ ) of all available vortex-shedding cycles have gone into averaged phase  $\bar{\theta}_i$ . The resulting phase-averaged  $\langle A_w \rangle_z$ -scaled PDF distributions at the off-centerline sampling location  $(x, y) = (3, 0.5)$  are shown in Fig. 15. Direct time-averaging of the  $\langle A_w \rangle_z$ -scaled PDF distributions (black solid line) already detects the presence, at the sampling location, of three-dimensional structures of size distributed around  $\lambda_z = 0.234$ . Furthermore, the evolution of the phase-averaged spanwise size distributions corroborates the observations made for the particular vortex-shedding cycle of Fig. 14. Three-dimensionality is scarce at phase  $\theta_0$ , but spanwise structures start appearing with quickly growing probability that peaks at  $\bar{\theta}_2$  with prevailing spanwise size  $\lambda_z \simeq 0.204$ . Structures become less abundant and/or less energetic for phases  $\bar{\theta}_3 \sim \bar{\theta}_4$  as they grow in typical size to  $\lambda_z \simeq 0.219$ . As the cycle progresses, spanwise structures are fast re-energized and become

more recurrent until reaching a new probability peak at phase  $\bar{\theta}_5$  with spanwise size distributed around  $\lambda_z \simeq 0.280$ . Beyond this point, ubiquity of three-dimensional structures sharply drops until becoming almost imperceptible at phase  $\bar{\theta}_6$ . Three-dimensionality remains insignificant for the rest of the cycle.

Spanwise-averaged flow vorticity snapshots taken at phases  $\theta_0, \theta_2$ , and  $\theta_5$  are shown in Fig. 16 to identify the location along the wake where three-dimensional structures occur. Phase-averaged snapshots [Fig. 16(b)] are shown alongside instantaneous snapshots [Fig. 16(a)], for the particular vortex-shedding cycle depicted in Fig. 14(b)] to convey the general recurrence of three-dimensionality at the same locations in the wake. The leading front of the Kármán vortex and the nearly quiescent flow field immediately downstream (top panel, which corresponds to phase  $\theta_0$ ) preserve a markedly two-dimensional character. In the downstream portion of the braid region, immediately at the vortex trailing front (middle panels,  $\theta_2$ ), is where the smallest highly energetic three-dimensional structures are to be identified. At the upstream part of the braid region, where it connects with the next Kármán vortex of opposite sign (bottom panels,  $\theta_5$ ), high energy spanwise structures of a slightly larger spanwise extent thrive. In between, in the mid-section of the braid region, three-dimensionality appears to be somewhat weaker. As a matter of fact, this is the result of the curved nature of the braid region such that its core sheet crosses the sampling location, at a fixed cross-stream coordinate, twice. It is natural to assume that the three-dimensional structures extend in fact along the braid region pretty much unaltered, just with a mild propensity to grow from the leading to trailing region. The apparent weakening would therefore be a result of the curvature of three-dimensional structures along the braids. This scrutiny of spanwise flow structures confirms the notion, already anticipated by the analysis of the primary and secondary flows, that three-dimensionality is suppressed by the strong spanwise vorticity of Kármán vortices but thrives in the trailing braid regions at a phase of  $225^\circ$  later, the precise phase lag that separates the most energetic spanwise structures ( $\theta_5$ ) from the weakest ( $\theta_0$ ). The inquiry into the spanwise length scale of three-dimensionality further reveals that the structures are of rather small spanwise extent and that their size experiences a periodic evolution along the vortex street.

Figure 17 shows instantaneous streamwise cross sections of cross-stream vorticity  $\omega_y(3, y, z)$ , containing the probe array (dashed line), at the very same times as in Fig. 16(a). The probe clearly registers quasi-two-dimensional flow at  $\theta_0$  (left panel), although three-dimensional structures are clearly visible at the symmetric  $y$ -location as a lower braid traverses the cross section at the time. At  $\theta_2$  (center panel), the upper braid downstream region traverses the cross section. In this case, a couple of vortex pairs are spotted at precisely the probe-array location. Note that a Fourier transform or signal autocorrelation along the probe would have provided the spacing between the vortex pairs rather than the local size of each one of them. The Hilbert transform works locally and will in fact produce the characteristic size of every strong vortex traversing the probe array. It must be realized that the sizes given by the Hilbert transform will correspond to that of a compact vortex pair. If, for whatever reason, the vortex pair splits into two counter-rotating vortices that drift apart, the Hilbert transform will measure the size of the original vortex pair as though the vortices had remained packed together. We thus measure double the size of individual vortices, regardless of

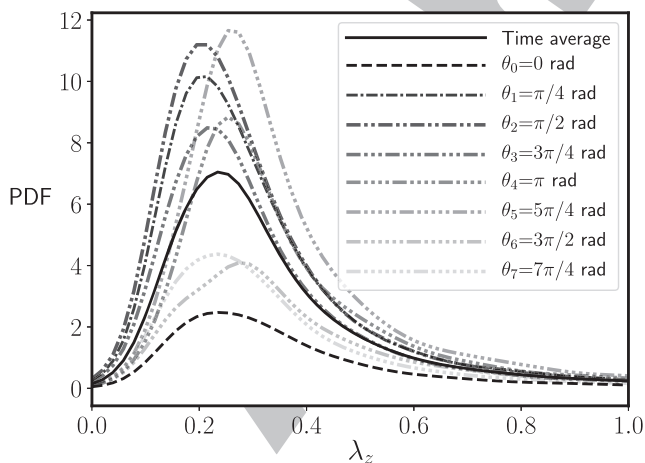


**FIG. 15.** Time-averaged (solid line) and phase-averaged (dashed lines, coloring as indicated in the legend)  $\langle A_w \rangle_z$ -scaled PDF distributions at phases  $\theta_i = 2\pi i/8$ . Normal/Gaussian kernel density estimation with a bandwidth  $\Delta z = 0.04$  has been employed.

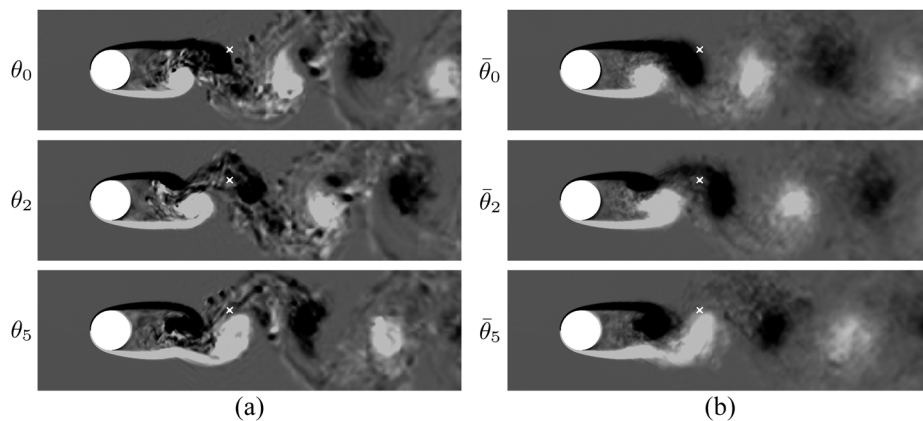


**FIG. 16.** Spanwise-averaged vorticity fields at phases  $\theta_0$  (top),  $\theta_2$  (middle), and  $\theta_5$  (bottom) along the vortex-shedding cycle. Vorticity is in the range  $\omega_z \in [-2, 2]$ , clear for positive and dark for negative. The cross indicates the sampling location of the signals in Fig. 14. (a) Instantaneous snapshots corresponding to the vortex-shedding cycle of Fig. 14(b). (b) Phase-averaged snapshots.

1161  
1162  
1163  
1164  
1165  
1166  
1167  
1168  
1169  
1170

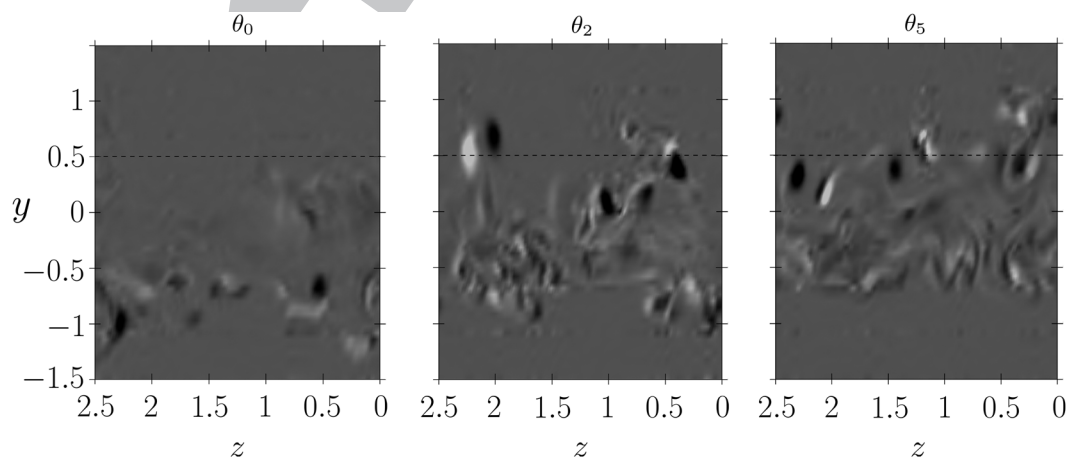
1140 whether they appear in pairs or in isolation. At  $\theta_5$  (right panel), it  
1141 is the upstream region of the braid that traverses the cross section.  
1142 Once more, both vortex pairs and isolated vortices can indistinctly  
1143 be detected at the probe array height.

1144 At the same height but below the wake center plane (i.e., the  
1145 mirror image of the probe location), three-dimensionality is weaker  
1146 and less structured than in the braid core, where the strongest vor-  
1147 tical structures of clear-cut characteristic size happen to be. We sur-  
1148 mise that it is these latter vortices that extract energy from the main  
1149 shear and constitute the primal instability that then breaks down  
1150 into the featureless lower-intensity turbulence that dominates the  
1151 trailing region left behind by the braids in their downstream advec-  
1152 tion. The low-intensity turbulent region in the bottom half of the  $\theta_2$   
1153 and  $\theta_5$  panels would therefore correspond to the region just cleared  
1154 by a lower braid and waiting to be reached by the leading front of an  
1155 oncoming Kármán vortex. A couple of final considerations regard-  
1156 ing structure size measurement need to be mentioned at this point.  
1157 First, if we consider vortex pairs as embedded inside an envelope,  
1158 the instantaneous horizontal size of this envelope as measured at the

1171 probe array will oscillate as the vortex, which has a certain stream-  
1172 wise tilt due to the braid slope and curvature, traverses it. From the  
1173 probe, the vortex pair will be seen as either rising or descending and  
1174 the correct size will only be measured when the vortex cores are  
1175 at exactly the probe height. This introduces a bias in size measure-  
1176 ment toward somewhat smaller-than-actual structures. A spanwise  
1177 tilt of a vortex pair will entail a similar effect. We have employed  $\bar{\omega}_y$   
1178 instead of the real vorticity  $\omega_y$  for computing structure size. There  
1179 is no guarantee that the sizes measured will remain the same if differ-  
1180 ent signals are used. Trading some vorticity component for another  
1181 or for any velocity component might produce different results. Devi-  
1182 ations should not be enormous, but the definition of structure size  
1183 is somewhat loose and can of course depend on the field used for its  
1184 measurement.

1171  
1172  
1173  
1174  
1175  
1176  
1177  
1178  
1179  
1180  
1181  
1182  
1183  
1184  
1185  
1186  
1187  
1188  
1189

1185 In order to characterize the typical spanwise size of three-  
1186 dimensional flow structures, the mode (peak) of the time-averaged  
1187  $\langle A_\omega \rangle_z$ -scaled  $\lambda_z$ -PDF distribution, rather than the mean, has been  
1188 taken as the most probable wavelength  $\bar{\lambda}_z$ . Due to the skewed  
1189 shape of the size distributions, the mean is not a particular good



1159 **FIG. 17.** Colormaps on a streamwise cross section, containing the probe array, of instantaneous cross-stream vorticity  $\omega_y(3, y, z)$  at phases  $\theta_0$ ,  $\theta_2$ , and  $\theta_5$ . The probe array  
1160 is indicated with a dashed line.

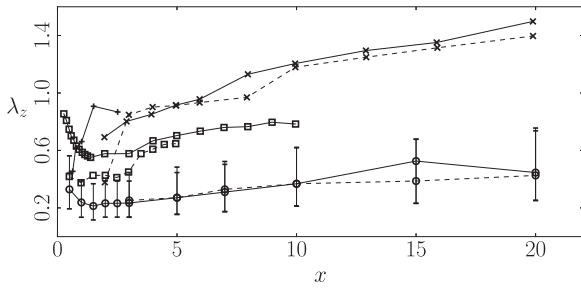


**FIG. 18.** Typical spanwise size  $\lambda_z$  of three-dimensional structures along the wake measured off-centerline at cross-stream locations  $y = 0.5$  (solid lines) and  $y = 1$  (dashed lines). Shown are our numerical results (circles) along with the numerical results by Gsell *et al.*<sup>36</sup> at  $Re = 3900$  (squares) and experimental results by Mansy *et al.*<sup>33</sup> at  $Re = 600$  (crosses) and Chyu and Rockwell<sup>37</sup> at  $Re = 10\,000$  (plus signs). The error bars denote the range for which the probability remains above half the peak probability.

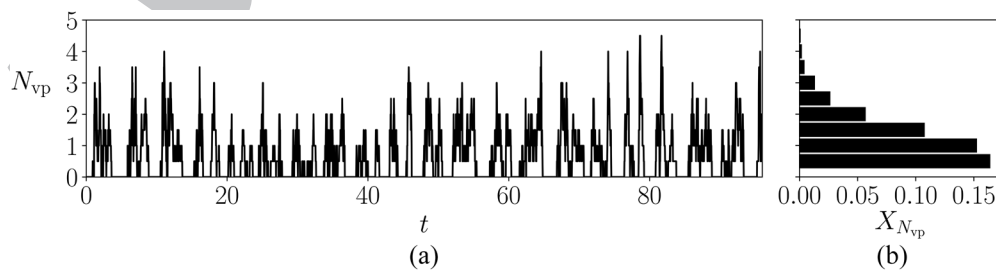
indicator of the most probable spanwise sizes. To provide a measure of distribution spread or variability, a range  $[\lambda_z^{\min}, \lambda_z^{\max}]$  has been defined by picking the interval where the PDF remains above 50 of its maximum. Thus, typical positive and negative deviations have been defined as  $\delta_{\lambda_z}^+ = \lambda_z^{\max} - \bar{\lambda}_z$  and  $\delta_{\lambda_z}^- = \bar{\lambda}_z - \lambda_z^{\min}$ , respectively.

Figure 18 shows the evolution of the typical spanwise size of three-dimensional structures along the wake. The measurements have been taken off-centerline at  $y = 0.5$  and  $y = 1$ . The trends for  $y = 0.5$  observed by Gsell *et al.*<sup>38</sup> at  $Re = 3900$  using a similar analysis are recovered in the present results at  $Re = 2000$ , although the typical sizes were notably larger in the former study. In our case, the spanwise size of structures decreases from  $\bar{\lambda}_z \approx 0.35$  in the immediate vicinity of the cylinder along the shear layers until reaching a minimum  $\bar{\lambda}_z \approx 0.25$  at about  $x \approx 2-3$  in the vortex formation region. The size gradually recovers afterward, asymptotically tending to  $\bar{\lambda}_z \approx 0.4$  by  $x = 20$ . In Ref. 38, the sizes are off by over 0.4. At  $y = 1$ , we observe the same trends as for  $y = 0.5$  and very close values from  $x \gtrsim 2.5$  on. In contrast with the observations by Gsell *et al.*<sup>38</sup> at the larger  $Re = 3900$ , the sizes of the structures in the very near wake at this cross-stream location are meaningless as three-dimensionality is barely noticeable. This can be ascribed to the lower  $Re$  employed in our simulations. Three-dimensionality (and turbulence, for that

matter) seems to have a hard time diffusing upstream and cross-stream at  $Re = 2000$  but not so much at  $Re = 3900$ . Comparison with the experimental results by Mansy *et al.*<sup>33</sup> at  $Re = 600$  and Chyu and Rockwell<sup>37</sup> at  $Re = 10\,000$  is hindered by the exceedingly different flow regimes considered and by the methodology employed, which we assess adequate for estimating spanwise structure spacing but not size. To any rate, Mansy *et al.*<sup>33</sup> reported a spanwise size  $\bar{\lambda}_z \approx 0.45$  at  $(x, y) = (3, 0.5)$ , which is larger but not overly far from our values at the same location.

#### D. Spanwise spacing of streamwise vortices in the near-wake

If the three-dimensional structures were to appear in a (pseudo-)periodic spanwise pattern, one would expect to observe  $N_{vp} \approx L_z/\lambda_z$  equispaced vortex pairs filling the entire spanwise extent of the domain. As we have seen, this is not the case and vortex pairs appear entirely decorrelated from one another and vortices in isolation are oftentimes observed. Figure 19(a) shows the instantaneous count of vortex pairs  $N_{vp}$  as a function of time. Vortices are counted whenever cross-stream pseudo-vorticity exceeds a certain threshold  $|\bar{\omega}_y| \geq 8$  at the designated location, here  $(x, y) = (3, 0.5)$ . In some periods, corresponding to the traversal of Kármán vortices, no streamwise vortices are observed at all. Along the braids, isolated streamwise vortices and vortex pairs are regularly detected instead. Up to 4–4.5 simultaneous vortex pairs have been detected occasionally such that the average spanwise spacing between side-by-side pairs is  $L_z/N_{vp} = 0.56-0.63$ . This minimum average spacing is well above the typical vortex-pair spanwise size  $\lambda_z^{\max}$  reported above such that not even in these rare occasions do the three-dimensional structures appear in anything remotely resembling a periodic pattern like that observed for the A and B modes at much lower Reynolds numbers. Figure 19(b) presents in a histogram, the fraction of time  $X_{N_{vp}}$  that the probe array at  $(x, y) = (3, 0.5)$  detects so many ( $N_{vp}$ ) simultaneous vortex pairs. Note that the unit is the vortex pair such that a vortex in isolation is counted as 1/2 and  $N_{vp}$  must necessarily take values that are a natural multiple of 0.5. Isolated vortices ( $N_{vp} = 0.5$ ) cross the probe array just over 15 of the time and close to another 15 of the time a vortex pair (or two isolated vortices,  $N_{vp} = 1$ ) is being detected. Larger amounts of simultaneous vortices are detected with decreasing probability. We are interested here in the continuous probability distribution of vortex spanwise spacing  $l_z$  in the case of the infinitely long cylinder, which is related to



**FIG. 19.** Count of vortex pairs traversing the probe array at  $(3, 0.5)$ . (a) Time evolution of the vortex pair count. The threshold for counting the occurrence of a vortex is  $|\bar{\omega}_y| \geq 8$ . (b) Histogram of time fraction  $X_{N_{vp}} \equiv t_{N_{vp}}/T$  of observation of  $N_{vp}$  vortex pairs. Half values result from the detection of isolated vortices.

1263 the number of vortices in a sufficiently extended cylinder of span-  
 1264 wise size  $L_z$  by  $l_z \equiv L_z/(2N_{vp})$ . While the maximum of the PDF for  $l_z$   
 1265 ( $l_z^{\max}$ ) is expected to be independent of  $L_z$  for sufficiently long cylin-  
 1266 ders, the maximum of the  $N_{vp}$ -PDF ( $N_{vp}^{\max}$ ) is instead foreseen as  
 1267 inversely proportional to the domain size. To properly reproduce the  
 1268 continuous distribution of  $l_z$  with a finite-span domain, one would  
 1269 naturally require that  $L_z$  is large enough so that the discrete dis-  
 1270 tribution of  $N_{vp}$  contains the maximum  $N_{vp}^{\max}$  and the probability  
 1271 tails drop sufficiently at either side. The maximum can be inter-  
 1272 preted as the preferred spanwise spacing of three-dimensional struc-  
 1273 tures in the cylinder wake and, as such, acts as a threshold to how  
 1274 many streamwise vortices can comfortably be packed together per  
 1275 unit span. Below this spacing, streamwise vortices tend to *repel* each  
 1276 other by whatever mechanism, possibly unaccounted for large-scale  
 1277 motions. In this sense, a strict minimum  $L_z$  should at the very least  
 1278 fit  $l_z^{\max} = L_z/(2N_{vp}^{\max})$ . In our domain  $L_z = 2.5$ , the probability of  
 1279 observation of simultaneous vortices is a strictly decreasing func-  
 1280 tion of the number considered, with  $N_{vp}^{\max} = 0.5$  corresponding to  
 1281 maximum probability. This would in principle point at an insuffi-  
 1282 cient domain size, but, as it happens,  $L_z = 2.5$  seems to be about  
 1283 the minimum that captures the probability distribution correctly up  
 1284 to the maximum, as the saturating value of  $X_{N_{vp}}$  for  $N_{vp}^{\max} = 0.5$   
 1285 seems to indicate. Larger domains would therefore properly capture  
 1286 the probability maximum and part of the decreasing trend toward  
 1287 lower  $N_{vp}$ , while smaller domains would be forcing the maximum  
 1288 to be at lower spacing values than the cylinder wake would naturally  
 1289 select. We believe that this may be among the reasons why insuffi-  
 1290 cient spanwise domain sizes produce wrong turbulent statistics, here  
 1291 and in published literature results. The spanwise spacing of vortical  
 1292 streamwise structures, rather than their size, would therefore dic-  
 1293 tate the minimum computational domain extent. The spacing being  
 1294 a function of Reynolds number, no definite trend can be extracted  
 1295 from our computations, all of which correspond to the same unique  
 1296  $Re = 2000$ .

1297 **E. Fastest growing three-dimensional structures**

1298 The Floquet stability analysis of the time-periodic two-  
 1299 dimensional flow around the cylinder has been successfully  
 1300 employed in the past to pinpoint the  $Re$ -regime at which three-  
 1301 dimensionality kicks in Refs. 17 and 36. The leading eigenmodes  
 1302 found are consistent with mode A observed in experiments, and  
 1303 the hysteresis can be ascribed to the subcritical character of the  
 1304 bifurcation. Meanwhile, the existence of mode B has been tracked  
 1305 down via Floquet analysis to a secondary bifurcation of the already  
 1306 unstable two-dimensional periodic vortex-shedding regime.<sup>10</sup> These  
 1307 bifurcations introducing three-dimensionality to the flow occur in  
 1308 the range  $Re \in [188.5, 260]$ . If forced computationally to preserve  
 1309 two-dimensionality, vortex-shedding remains time-periodic for still  
 1310 some range of  $Re$ . At  $Re = 2000$ , however, periodicity has long  
 1311 been disrupted and two-dimensional vortex-shedding has become  
 1312 chaotic. It is highly debatable whether the Floquet analysis of the  
 1313 Kármán periodic solution at this regime can capture any of the fea-  
 1314 tures of the three-dimensional structures observed in experiments  
 1315 and in fully three-dimensional numerical simulations. Nonetheless,  
 1316 we have chosen here to undertake what we call pseudo-Floquet sta-  
 1317 bility analysis of the underlying two-dimensional solution, which  
 1318 happens to be a pseudo-periodic chaotic state, to compare the fastest

growing modes with the structures that arise in direct numerical  
 simulation. Long two-dimensional time integration has been per-  
 formed to characterize the chaotic state, with velocity and pres-  
 sure fields  $[\mathbf{u}_2^{2D}, p_2^{2D}](\mathbf{r}_2, t)$ . Random three-dimensional perturba-  
 tions  $\tilde{\mathbf{u}}$  of wavenumber  $\beta_z = 2\pi/\lambda_z$  ( $\lambda_z$  is the fundamental wave-  
 length), scaled to very low amplitude by a factor  $\epsilon \sim 10^{-12}$ , have been  
 added to  $\mathbf{u}_2^{2D}$  at several randomly picked time-instants and evolved  
 in time using a single spanwise Fourier mode in order to avoid  
 spanwise mode interaction and, thus, allow straightforward analy-  
 sis, through direct time evolution, of the modal growth/decay in  
 the linear regime. Since  $[\mathbf{u}_2^{2D}, p_2^{2D}]$  exactly satisfy the Navier–Stokes  
 equations, introducing the perturbed field

$$[\mathbf{u}, p](\mathbf{r}; t) = [\mathbf{u}_2^{2D}, p_2^{2D}](\mathbf{r}_2; t) + \epsilon[\tilde{\mathbf{u}}, \tilde{p}](\mathbf{r}; t)$$

results in

$$\frac{\partial \tilde{\mathbf{u}}}{\partial t} + (\mathbf{u}_2^{2D} \cdot \nabla) \tilde{\mathbf{u}} + (\tilde{\mathbf{u}} \cdot \nabla) \mathbf{u}_2^{2D} = -\nabla \tilde{p} + \frac{1}{Re} \nabla^2 \tilde{\mathbf{u}},$$

$$\nabla \cdot \tilde{\mathbf{u}} = 0,$$

where the nonlinear term  $(\tilde{\mathbf{u}} \cdot \nabla) \tilde{\mathbf{u}}$  has been dropped as negligible  
 from its appearing scaled by  $\epsilon^2$ .

If  $[\mathbf{u}_2^{2D}, p_2^{2D}]$  were exactly periodic, Floquet theory’s modal  
 ansatz would establish that, after some initial transients  $t_0$ , the  
 perturbation field should evolve as

$$[\tilde{\mathbf{u}}, \tilde{p}](\mathbf{r}; t_0 + kT) = [\tilde{\mathbf{u}}_0, \tilde{p}_0](\mathbf{r}) \exp(\sigma kT), \quad k \in \mathbb{N},$$

where  $T$  is the period of the two-dimensional periodic base flow and  
 $\mu \equiv \exp(\sigma T)$  is the leading multiplier, associated with the leading  
 eigenmode  $[\tilde{\mathbf{u}}_0, \tilde{p}_0]$ .

Here, the base flow is not periodic but chaotic and the evolu-  
 tion of the perturbation field cannot be expected to be exactly modal.  
 However, since two-dimensional chaotic vortex shedding retains a  
 high degree of periodicity, the time evolution of the perturbation  
 happens to be quasi-modal. Figures 20(a)–20(c) show an example of  
 the growth of the single Fourier mode with  $\beta_z = 20.94$  on top of the  
 chaotic two-dimensional base flow. A pseudo-periodic chaotic solu-  
 tion as we have has no unique period so that we choose to define it as  
 the flight time between consecutive crossings of a purposely devised  
 Poincaré section:  $T_k = t_k - t_{k-1}$ . In our case, the Poincaré section is  
 pierced by the phase map trajectory every time  $C_L = 0$  and  $dC_L/dt$   
 $< 0$ , as indicated by the dashed line and the circles in Fig. 20(a).  
 The kinetic energy  $E_{\beta_z}$  contained in the unique spanwise Fourier mode  
 employed in the simulation is shown in Fig. 20(b). After some initial  
 transients with a slight decrease, the modal energy starts increasing,  
 following an exponential trend for  $t \gtrsim 10$  until nonlinear saturation  
 occurs for  $t \gtrsim 30$ . The energy levels of the unique spanwise mode of  
 wavenumber  $\beta_z$  at the Poincaré crossings are marked with circles,  
 and the multipliers  $\mu_k$  estimated at crossing  $k$  from the energy ratio  
 between consecutive crossings  $k - 1$  and  $k$  as

$$\frac{E_{\beta_z}^k}{E_{\beta_z}^{k-1}} = \frac{\|\tilde{\mathbf{u}}^k\|_{L_2}^2}{\|\tilde{\mathbf{u}}^{k-1}\|_{L_2}^2} = \exp(2\sigma T_k) \equiv \mu_k^2,$$

where  $\|\cdot\|_{L_2}$  denotes the  $L_2$  norm, are plotted in Fig. 20(c). As  
 expected for an unstable base flow, the multiplier is greater than  
 unity, but unlike what happens for an exactly periodic base flow,  
 its value is variable along the evolution. In the case of our chaotic

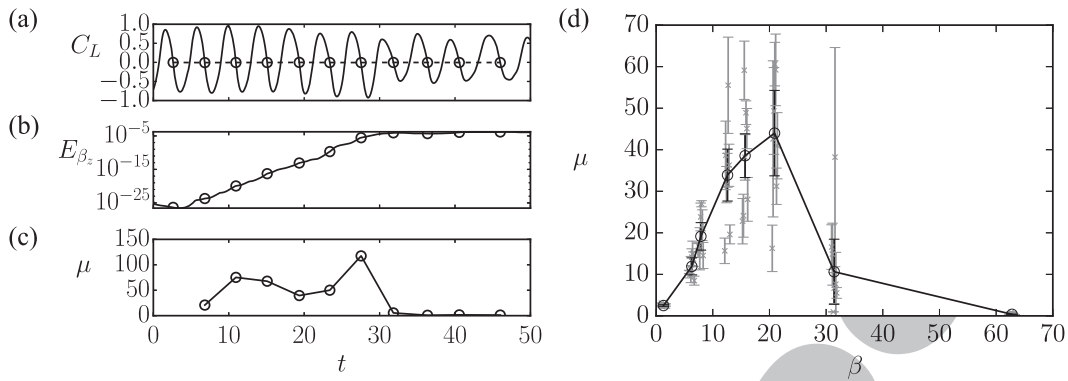


**FIG. 20.** Quasi-modal evolution of a perturbation with  $\beta_z = 2\pi/\lambda_z = 20.94$  ( $\lambda_z = 0.3$ ) on two-dimensional chaotic vortex shedding at  $Re = 2000$ . (a) Time evolution of  $C_L$  as used to define a Poincaré section (Poincaré crossing marked with circles). (b) Evolution of the perturbation field kinetic energy. (c) Evolution of the multiplier as computed for every two consecutive Poincaré crossings. (d) Value of the multiplier  $\mu$  as a function of spanwise wavenumber  $\beta_z$ . Seven different initial conditions for the chaotic base flow result in the multiple sets of data for each  $\beta_z$  (gray). All seven are gathered in a unique curve (black line). Error-bars indicate the variability of the multiplier in time.

two-dimensional vortex shedding, the variability of the multiplier is rather large.

Up to seven different initial base state conditions along the two-dimensional chaotic vortex shedding evolution have been taken and tested for spanwise wavelengths in the range  $\lambda_z \in [0.1, 10]$ , corresponding to wavenumbers  $\beta_z \in [0.628, 62.8]$ . The results for the seven individual samples are shown in Fig. 20(d) as gray crosses with error-bars, which indicate the mean and standard deviation of the multiplier along the time evolution, respectively. In some cases, the fluctuation is small, corresponding with initial conditions at a stage of the time evolution where vortex-shedding is particularly well behaved. In others, the variability is huge. Averaging the probability distribution of  $\mu$  across samples reduces the variability in the multiplier to some extent and produces a softer dependence of the multiplier on the wavenumber. The maximum growth of infinitesimal three-dimensional perturbations seems to occur for spanwise wavenumbers  $\beta_z \approx 20.94$ , which corresponds to a spanwise wavelength of  $\lambda_z = 2\pi/\beta_z \approx 0.3$ . This wavelength is in good agreement with

the spanwise size of the structures we observe in the wake region in fully three-dimensional turbulent simulations, particularly so in the very near-wake region at  $(x, y) = (0.5, 0.5)$ .

A snapshot of the fastest growing (leading) eigenmode, taken at the time of a Poincaré crossing within the linear regime, is depicted in Fig. 21(b), while Fig. 21(a) shows the instantaneous two-dimensional state at the exact same time. The spanwise vorticity ( $\omega_z$ ) colormap indicates that the mode is at its strongest along the braid region that connects the newly forming Kármán vortex core in the immediate vicinity of the cylinder and the preceding vortex of the same sign. The instability is local in the sense that exponential growth occurs only at a very precise location within the wake formation region and does not extend to the region where the wake is already in place and the Kármán vortex street is well developed. Infinitesimal perturbations of spanwise wavelength  $\lambda_z = 2\pi/\beta_z$  therefore exponentially grow only within the most recently generated braid at all times. There is no guarantee that the perturbation reaches nonlinear saturation unaltered and thus constitutes the origin of the three-dimensional structures observed in experiments and direct numerical simulation, but they certainly have the right spanwise size and are located in the precise flow regions where the structures thrive. This gives an indication that the structures observed in the wake at these transitional regimes might bear a strong connection with the fastest growing mode on the underlying two-dimensional base flow.

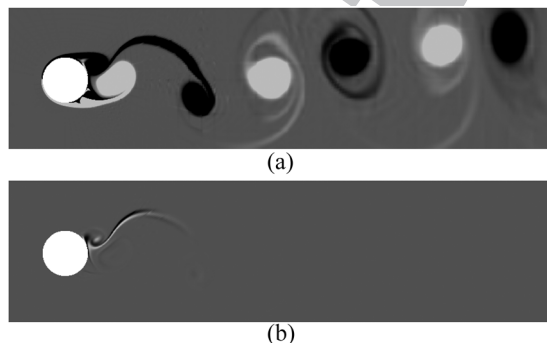


**FIG. 21.** Spanwise vorticity ( $\omega_z$ ) colormaps at the Poincaré section defined by  $C_L = 0$  and  $dC_L/dt < 0$  of (a) the two-dimensional chaotic vortex shedding solution ( $\omega_z \in [-2, 2]$ ) and (b) the leading eigenmode (arbitrary symmetric  $\omega_z$ , range) for  $\beta_z = 20.94$ .

**V. CONCLUSIONS**

A comprehensive numerical study of the transitional flow past a circular cylinder at  $Re = 2000$  has been performed in order to characterize the three-dimensional flow structures that appear in the wake. Domains smaller than  $L_z < 2.5$  in the spanwise direction fail to yield correct flow statistics, possibly due to the existence of unaccounted-for large-scale motions that are precluded by a limited size.

By thoroughly analyzing flow statistics and wake topology, we settle the controversy regarding the U- vs V-shaped streamwise

1429 velocity mean profile in the near-wake and explain the observa- 1485  
 1430 tion of one or the other as the result of taking measurements at 1486  
 1431 a fixed streamwise location. Correcting the probe location accord- 1487  
 1432 ing to recirculation bubble size allows recasting the same results for 1488  
 1433 comparison with experiments at different Reynolds numbers. Very 1489  
 1434 good agreement with literature results is thus found across a range 1490  
 1435 of Reynolds numbers within the transitional regime for all sorts of 1491  
 1436 flow statistics. 1492

1437 Sufficiently long time series have allowed for the detection 1493  
 1438 of the occasional manifestation of a Kelvin–Helmholtz instability 1494  
 1439 within the shear layers that originate from the detachment of the 1495  
 1440 boundary layers at either side of the cylinder and flap synchronous to 1496  
 1441 the generation of Kármán vortices. At  $Re = 2000$ , Kelvin–Helmholtz 1497  
 1442 vortices have been observed from time to time, with a frequency 1498  
 1443 of  $f_{KH} \simeq 0.84$  that closely matches experimental observation and 1499  
 1444 the trends derived from first principles and scaling/dimensional 1500  
 1445 analysis. The instability appears as a broad band peak in the spec- 1501  
 1446 trum of any velocity signal measured in the cylinder near-wake, and 1502  
 1447 the associated spanwise vortices feature a certain spanwise local- 1503  
 1448 ization in contrast with the spanwise-independent nature of the 1504  
 1449 inviscid Kelvin–Helmholtz instability of a perfectly parallel shear 1505  
 layer. 1506

1450 As a first approach to characterizing the three-dimensionality 1507  
 1451 in the wake, the flow has been decomposed into a primary two- 1508  
 1452 dimensional signal and a secondary signal containing the remaining 1509  
 1453 three-dimensional structure. This has led to the observation that 1510  
 1454 three-dimensionality occurs primarily in the braid region and attains 1511  
 1455 its maximum with a phase lag of approximately  $5/8$  rad with respect 1512  
 1456 to the maximum of the primary flow at any given location along the 1513  
 1457 wake, which corresponds to the passage of a Kármán vortex. 1514

1458 To further investigate the features of the three-dimensional 1515  
 1459 structures that appear in the wake, the Hilbert transform of a signal 1516  
 1460 along a spanwise probe array has been employed to derive instan- 1517  
 1461 taneous spanwise size distributions of vortical structures and phase- 1518  
 1462 averaging has been conducted to analyze the evolution of the dis- 1519  
 1463 tributions along the vortex-shedding cycle. We have found that the 1520  
 1464 most energetic spanwise-localized structures correspond to the pas- 1521  
 1465 sage of a braid through the probe location. The maximum occurs 1522  
 1466 twice along a vortex-shedding cycle due to the arched shape of the 1523  
 1467 braid, and the most probable size of the structures is found to be 1524  
 1468 around  $\lambda_z \simeq 0.20$ – $0.28$  at  $(x, y) = (3, 0.5)$ , the smaller sizes corre- 1525  
 1469 sponding to the leading and the larger sizes corresponding to the 1526  
 1470 trailing regions of the braid, respectively. We have measured the typ- 1527  
 1471 ical structure size at different locations along the wake and found 1528  
 1472 that after a fast drop in the very near wake, the sizes start growing 1529  
 1473 progressively for  $x > 2.5$  and asymptotically reach a maximum of 1530  
 1474  $\lambda_z = 0.4$  for  $\lambda_z > 20$ . While the sizes are found to be significantly 1531  
 1475 smaller than those reported in experimental and numerical results 1532  
 1476 at  $Re = 3900$ , the trends are similar. No difference has been found 1533  
 1477 between measurements with probes at  $y = 0.5$  and  $y = 1$ , except 1534  
 1478 that the latter does not register significant three-dimensionality 1535  
 for  $x < 3$ . 1536

1479 By analyzing the typical spanwise spacing among streamwise 1537  
 1480 vortices, we have observed that the most frequent vortex-pair count 1538  
 1481 in our  $L_z = 2.5$  domain is  $N_{vp}^{\max} = 0.5$  (an isolated vortex), followed 1539  
 1482 closely by 1 (two vortices or a vortex pair), corresponding to most 1540  
 1483 probable average spacings  $l_z^{\max} \simeq 2.5$  and  $1.25$ , respectively. This 1541  
 1484 seems to indicate that our domain properly captures the spacing 1542

distribution up to its maximum and that shorter domains would 1485  
 tend to artificially squeeze the three-dimensional structures into 1486  
 spanwise extents that would not be selected naturally in the limit of 1487  
 very long cylinders. We believe that this might be one of the reasons 1488  
 behind the failure of small spanwise domains to produce correct tur- 1489  
 bulent wake statistics, but the ultimate culprit, possibly related to 1490  
 the existence of large-scale motions of this length scale, remains a 1491  
 mystery. 1492

1493 To try and understand the origin of the three-dimensional 1494  
 1495 structures observed in the wake, we have analyzed the growth, in the 1496  
 1497 linear regime, of quasi-modal perturbations added to the underlying 1498  
 1499 two-dimensional chaotic vortex-shedding flow. The fastest growing 1500  
 1501 perturbations happen to be localized in the braid region that 1502  
 1503 connects the last forming Kármán vortex with the immediately pre- 1504  
 1505 ceding one, and they have a spanwise wavelength of  $\lambda_z \simeq 0.3$ . The 1506  
 1507 close coincidence in the size and location of these quasi-modal per- 1508  
 1509 turbations with the three-dimensional structures observed in direct 1509  
 1510 numerical simulation points at a close relation. We surmise that 1511  
 1512 the latter are the result of the nonlinear saturation of the former, 1512  
 1513 although the interactions among the full range of unstable leading 1513  
 1514 eigenmodes as well as the distance from the critical Reynolds num- 1514  
 1515 ber at which the instabilities occur in the first place render it difficult 1515  
 to establish a direct connection between the linear and nonlinear 1516  
 regimes. 1517

## 1518 ACKNOWLEDGMENTS

1519 This work was financed by the Spanish and Catalan Govern- 1510  
 1520 ments under Grant Nos. FIS2016-77849-R and 2017-SGR-00785, 1511  
 1521 respectively. The authors also thankfully acknowledge the computer 1512  
 1522 resources at MareNostrum and Calendula accessed through Grant 1513  
 1523 Nos. RES-FI-2017-2-0020 and RES-FI-2017-3-0009, respectively. 1514

1515 The authors declare no conflict of interest. 1516

## 1517 DATA AVAILABILITY

1518 The data that support the findings of this study are available 1517  
 1519 from the corresponding author upon reasonable request. 1518

## 1519 REFERENCES

- 1520 <sup>1</sup>C. H. K. Williamson, “Vortex dynamics in the cylinder wake,” *Annu. Rev. Fluid* 1521  
*Mech.* **28**, 477–539 (1996).
- 1522 <sup>2</sup>E. Berger and R. Wille, “Periodic flow phenomena,” *Annu. Rev. Fluid Mech.* **4**(1), 1523  
 313–340 (1972).
- 1524 <sup>3</sup>A. V. Dovgal, V. V. Kozlov, and A. Michalke, “Laminar boundary layer separa- 1525  
 tion: Instability and associated phenomena,” *Prog. Aeronaut. Sci.* **30**(1), 61–94  
 (1994).
- 1526 <sup>4</sup>R. L. Simpson, “Turbulent boundary-layer separation,” *Annu. Rev. Fluid Mech.* 1527  
**21**(1), 205–232 (1989).
- 1528 <sup>5</sup>M. M. Rai, “A computational investigation of the instability of the detached shear 1529  
 layers in the wake of a circular cylinder,” *J. Fluid Mech.* **659**, 375–404 (2010).
- 1530 <sup>6</sup>M. Thompson, K. Hourigan, and J. Sheridan, “Three-dimensional instabilities in 1531  
 the wake of a circular cylinder,” *Exp. Therm. Fluid Sci.* **12**(2), 190–196 (1996).
- 1532 <sup>7</sup>T. von Kármán, “Über den mechanismus des widerstandes, den ein bewegter 1533  
 körper in einer flüssigkeit erfährt,” *Nachr. Ges. Wiss. Göttingen Math.-Phys. Kl.* 1534  
**■**, 509–517 (1911).
- 1535 <sup>8</sup>T. von Kármán, “Über den mechanismus des widerstandes, den ein bewegter 1536  
 körper in einer flüssigkeit erfährt,” *Nachr. Ges. Wiss. Göttingen Math.-Phys. Kl.* 1537  
**■**, 547–556 (1912).

- 1538 <sup>9</sup>R. D. Henderson, “Details of the drag curve near the onset of vortex shedding,”  
1539 *Phys. Fluids* **7**(9), 2102–2104 (1995).
- 1540 <sup>10</sup>D. Barkley and R. D. Henderson, “Three-dimensional Floquet stability analysis  
1541 of the wake of a circular cylinder,” *J. Fluid Mech.* **322**, 215–241 (1996).
- 1542 <sup>11</sup>T. Sarpkaya, “Vortex-induced oscillations: A selective review,” *J. Appl. Mech.*  
1543 **46**(2), 241–258 (1979).
- 1544 <sup>12</sup>N. Ferguson and G. V. Parkinson, “Surface and wake flow phenomena of  
1545 the vortex-excited oscillation of a circular cylinder,” *J. Eng. Ind.* **89**(4), 831–838  
(1967).
- 1546 <sup>13</sup>C. H. K. Williamson and R. Govardhan, “Vortex-induced vibrations,” *Annu.*  
1547 *Rev. Fluid Mech.* **36**(1), 413–455 (2004).
- 1548 <sup>14</sup>J. C. Hardin and S. L. Lamkin, “Aeroacoustic computation of cylinder wake  
1549 flow,” *AIAA J.* **22**(1), 51–57 (1984).
- 1550 <sup>15</sup>M. S. Howe, *Frontmatter*, Cambridge Monographs on Mechanics (Cambridge  
1551 University Press, 1998), pp. i–vi.
- 1552 <sup>16</sup>C. H. K. Williamson, “Mode A secondary instability in wake transition,” *Phys.*  
1553 *Fluids* **8**(6), 1680–1682 (1996).
- 1554 <sup>17</sup>R. D. Henderson and D. Barkley, “Secondary instability in the wake of a circular  
1555 cylinder,” *Phys. Fluids* **8**(6), 1683–1685 (1996).
- 1556 <sup>18</sup>C. H. K. Williamson, “The existence of two stages in the transition to three-  
1557 dimensionality of a cylinder wake,” *Phys. Fluids* **31**(11), 3165–3168 (1988).
- 1558 <sup>19</sup>A. Roshko, “On the development of turbulent wakes from vortex streets,”  
1559 Technical Report 1191, National Advisory Committee for Aeronautics, 1954.
- 1560 <sup>20</sup>M. S. Bloor, “The transition to turbulence in the wake of a circular cylinder,”  
1561 *J. Fluid Mech.* **19**(2), 290–304 (1964).
- 1562 <sup>21</sup>C. H. K. Williamson, “The natural and forced formation of spot-like ‘vortex  
1563 dislocations’ in the transition of a wake,” *J. Fluid Mech.* **243**, 393–441  
(1992).
- 1564 <sup>22</sup>L. Schiller and W. Linke, “Druck- und reibungswiderstand des zylinders bei  
1565 Reynoldsschen zahlen 5000 bis 40000,” *Z. Flugtech. Motorluft.* **24**, 193–198  
(1933).
- 1566 <sup>23</sup>A. Prasad and C. H. K. Williamson, “The instability of the shear layer separating  
1567 from a bluff body,” *J. Fluid Mech.* **333**, 375–402 (1997).
- 1568 <sup>24</sup>C. H. K. Williamson, J. Wu, and J. Sheridan, “Scaling of streamwise vortices in  
1569 wakes,” *Phys. Fluids* **7**(10), 2307–2309 (1995).
- 1570 <sup>25</sup>T. Wei and C. R. Smith, “Secondary vortices in the wake of circular cylinders,”  
1571 *J. Fluid Mech.* **169**, 513–533 (1986).
- 1572 <sup>26</sup>A. Kourta, H. C. Boisson, P. Chassaing, and H. H. Minh, “Nonlinear interaction  
1573 and the transition to turbulence in the wake of a circular cylinder,” *J. Fluid Mech.*  
1574 **181**, 141–161 (1987).
- 1575 <sup>27</sup>C. Norberg, “Effects of Reynolds number and a low-intensity freestream turbu-  
1576 lence on the flow around a circular cylinder,” Technical Report 87/2, Chalmers  
1577 University, Göteborg, Sweden, 1987.
- 1578 <sup>28</sup>A. Prasad and C. H. K. Williamson, “The instability of the separated shear layer  
1579 from a bluff body,” *Phys. Fluids* **8**(6), 1347–1349 (1996).
- 1580 <sup>29</sup>A. Roshko, “Perspectives on bluff body aerodynamics,” *J. Wind Eng. Ind.*  
1581 *Aerodyn.* **49**(1), 79–100 (1993).
- 1582 <sup>30</sup>S. Szepeszy and P. W. Bearman, “Aspect ratio and end plate effects on vortex  
1583 shedding from a circular cylinder,” *J. Fluid Mech.* **234**, 191–217 (1992).
- 1584 <sup>31</sup>C. Norberg, “An experimental investigation of the flow around a circular  
1585 cylinder: Influence of aspect ratio,” *J. Fluid Mech.* **258**, 287–316 (1994).
- 1586 <sup>32</sup>C. H. K. Williamson, “Three-dimensional transition in the near wake of a  
1587 cylinder,” *Bull. Am. Phys. Soc.* **32**, 2098 (1987).
- 1588 <sup>33</sup>H. Mansy, P.-M. Yang, and D. R. Williams, “Quantitative measurements of  
1589 three-dimensional structures in the wake of a circular cylinder,” *J. Fluid Mech.*  
1590 **270**, 277–296 (1994).
- 1591 <sup>34</sup>H. Q. Zhang, U. Fey, B. R. Noack, M. König, and H. Eckelmann, “On the  
1592 transition of the cylinder wake,” *Phys. Fluids* **7**(4), 779–794 (1995).
- 1593 <sup>35</sup>J. Wu, J. Sheridan, M. C. Welsh, and K. Hourigan, “Three-dimensional vortex  
1594 structures in a cylinder wake,” *J. Fluid Mech.* **312**, 201–222 (1996).
- 1595 <sup>36</sup>B. R. Noack and H. Eckelmann, “A global stability analysis of the steady and  
1596 periodic cylinder wake,” *J. Fluid Mech.* **270**, 297–330 (1994).
- 1597 <sup>37</sup>C. K. Chyu and D. Rockwell, “Near-wake structure of an oscillating cylinder:  
1598 Effect of controlled shear-layer vortices,” *J. Fluid Mech.* **322**, 21–49 (1996).
- 38 S. Gsell, R. Bourguet, and M. Braza, “Three-dimensional flow past a fixed or  
freely vibrating cylinder in the early turbulent regime,” *Phys. Rev. Fluids* **3**, 013902  
(2018).
- 39 I. Wygnanski, F. Champagne, and B. Marasli, “On the large-scale structures  
in two-dimensional, small-deficit, turbulent wakes,” *J. Fluid Mech.* **168**, 31–71  
(1986).
- 40 W. K. George, “Asymptotic effect of initial and upstream conditions on turbu-  
lence,” *J. Fluids Eng.* **134**(6), 061203 (2012).
- 41 Y. Zhou and R. Antonia, “Effect of initial conditions on characteristics of  
turbulent far wake,” *JSME Int. J., Ser. B* **37**(4), 718–725 (1994).
- 42 G. L. Brown and A. Roshko, “Turbulent shear layers and wakes,” *J. Turbul.* **13**,  
N51 (2012).
- 43 S. L. Tang, R. A. Antonia, L. Djenidi, and Y. Zhou, “Complete self-preservation  
along the axis of a circular cylinder far wake,” *J. Fluid Mech.* **786**, 253–274  
(2016).
- 44 Y. Zhou, R. A. Antonia, and W. K. Tsang, “The effect of Reynolds number on a  
turbulent far-wake,” *Exp. Fluids* **25**(2), 118–125 (1998).
- 45 L. M. Lourenco and C. Shih, “Characteristics of the plane turbulent near wake  
of a circular cylinder, a particle image velocimetry study,” Taken from Beaudan  
and Moin<sup>50</sup>, 1993.
- 46 Y. Zhou and R. A. Antonia, “A study of turbulent vortices in the near wake of a  
cylinder,” *J. Fluid Mech.* **253**, 643–661 (1993).
- 47 L. Ong and J. Wallace, “The velocity field of the turbulent very near wake of a  
circular cylinder,” *Exp. Fluids* **20**(6), 441–453 (1996).
- 48 C. Norberg, “LDV-measurements in the near wake of a circular cylinder,”  
ASME Paper No. FEDSM98-521, 1998.
- 49 P. Parnaudeau, J. Carlier, D. Heitz, and E. Lamballais, “Experimental and  
numerical studies of the flow over a circular cylinder at Reynolds number 3900,”  
*Phys. Fluids* **20**(8), 085101 (2008).
- 50 P. Beaudan and P. Moin, “Numerical experiments on the flow past a circular  
cylinder at sub-critical Reynolds number,” Technical report, NASA STI/Recon  
Technical Report ■, December 1994.
- 51 R. Mittal, “Progress on LES of flow past a circular cylinder,” Technical report ■,  
Center for Turbulence Research, 1996.
- 52 M. Breuer, “Large eddy simulation of the subcritical flow past a circular cylinder:  
Numerical and modeling aspects,” *Int. J. Numer. Methods Fluids* **28**(9), 1281–  
1302 (1998).
- 53 X. Ma, G.-S. Karamanos, and G. E. Karniadakis, “Dynamics and low-dimen-  
sionality of a turbulent near wake,” *J. Fluid Mech.* **410**, 29–65 (2000).
- 54 A. G. Kravchenko and P. Moin, “Numerical studies of flow over a circular  
cylinder at  $Re_D = 3900$ ,” *Phys. Fluids* **12**(2), 403–417 (2000).
- 55 J. Franke and W. Frank, “Large eddy simulation of the flow past a circular  
cylinder at  $Re = 3900$ ,” *J. Wind Eng. Ind. Aerodyn.* **90**(10), 1191–1206  
(2002).
- 56 O. Lehmkuhl, I. Rodríguez, R. Borrell, and A. Oliva, “Low-frequency unsteadiness  
in the vortex formation region of a circular cylinder,” *Phys. Fluids* **25**(8),  
085109 (2013).
- 57 C. Norberg, “Fluctuating lift on a circular cylinder: Review and new measure-  
ments,” *J. Fluids Struct.* **17**(1), 57–96 (2003).
- 58 E. Konstantinidis, S. Balabani, and M. Yianneskis, “The effect of flow pertur-  
bations on the near wake characteristics of a circular cylinder,” *J. Fluids Struct.*  
**18**(3-4), 367–386 (2003).
- 59 E. Konstantinidis, S. Balabani, and M. Yianneskis, “Conditional averaging of  
PIV plane wake data using a cross-correlation approach,” *Exp. Fluids* **39**(1), 38–47  
(2005).
- 60 E. Konstantinidis and S. Balabani, “Flow structure in the locked-on wake of a  
circular cylinder in pulsating flow: Effect of forcing amplitude,” *Int. J. Heat Fluid  
Flow* **29**(6), 1567–1576 (2008).
- 61 S. Dong, G. E. Karniadakis, A. Ekmekci, and D. Rockwell, “A combined direct  
numerical simulation-particle image velocimetry study of the turbulent near  
wake,” *J. Fluid Mech.* **569**, 185–207 (2006).
- 62 H. Ouvrard, B. Koobus, A. Dervieux, and M. V. Salvetti, “Classical and varia-  
tional multiscale LES of the flow around a circular cylinder on unstructured grids,”  
*Comput. Fluids* **39**(7), 1083–1094 (2010).

- 1658 <sup>63</sup>I. Afgan, Y. Kahil, S. Benhamadouche, and P. Sagaut, "Large eddy simulation  
1659 of the flow around single and two side-by-side cylinders at subcritical Reynolds  
1660 numbers," *Phys. Fluids* **23**(7), 075101 (2011). 1678
- 1661 <sup>64</sup>H. Chen, Z. Li, and Y. Zhang, "U or V shape: Dissipation effects on cylinder flow  
1662 implicit large-eddy simulation," *AIAA J.* **55**(2), 459–473 (2016). 1679
- 1663 <sup>65</sup>F. Tremblay, "Direct and large-eddy simulation of flow around a circular  
1664 cylinder at subcritical Reynolds numbers," Ph.D. thesis, Technische Universität  
1665 München, 2002. 1680
- 1666 <sup>66</sup>R. Mittal, "Large-eddy simulation of flow past a circular cylinder," Technical  
1667 report ■, Center for Turbulence Research, 1995. 1681
- 1668 <sup>67</sup>A. H. Mohammad, Z. J. Wang, and C. Liang, "Large eddy simulation of flow  
1669 over a cylinder using high-order spectral difference method," *Adv. Appl. Math.*  
1670 *Mech.* **2**(4), 451–466 (2010). 1682
- 1671 <sup>68</sup>G. Lodato and A. Jameson, "LES modeling with high-order flux reconstruction  
1672 and spectral difference schemes," in *ICCFD7 Conference 2012* (■, 2012), Vol. 2201,  
pp. 9–13. 1683
- 1673 <sup>69</sup>J. G. Wissink and W. Rodi, "Numerical study of the near wake of a circular  
1674 cylinder," *Int. J. Heat Fluid Flow* **29**(4), 1060–1070 (2008). 1684
- <sup>70</sup>R. D. Peltzer, "The effect of upstream shear and surface roughness on  
the vortex shedding patterns and pressure distributions around a circular  
in transitional Reynolds number flows," M.Sc. thesis, VPI and SU, 1980,  
<https://ci.nii.ac.jp/naid/10010461630/en/>. 1675
- <sup>71</sup>H. G.-C. Woo, J. A. Peterka, and J. E. Cermak, "Experiments on vortex shedding  
from stationary and oscillating cables in a linear shear flow," Technical report ■,  
Colorado State University, Libraries, 1981. 1676
- <sup>72</sup>J. H. Gerrard, "Experimental investigation of separated boundary layer under-  
going transition to turbulence," *Phys. Fluids* **10**(9P2), S98 (1967). 1677
- <sup>73</sup>A. Prasad and C. H. K. Williamson, "Three-dimensional effects in turbulent  
bluff-body wakes," *J. Fluid Mech.* **343**, 235–265 (1997). 1678
- <sup>74</sup>C. D. Cantwell, D. Moxey, A. Comerford, A. Bolis, G. Rocco, G.  
Mengaldo, D. De Grazia, S. Yakovlev, J.-E. Lombard, D. Ekelschot, B. Jordi, H. Xu,  
Y. Mohamied, C. Eskilsson, B. Nelson, P. Vos, C. Biotto, R. M. Kirby, and S. J.  
Sherwin, "Nektar++: An open-source spectral/hp element framework," *Comput.*  
*Phys. Commun.* **192**, 205–219 (2015). 1679
- <sup>75</sup>C. H. K. Williamson, "Three-dimensional wake transition," *J. Fluid Mech.* **328**,  
345–407 (1996). 1680